Retention mechanisms of stable- and radioactive- Cs and Sr in geopolymer materials: Insights into gel structural evolution and leaching behavior

Guiyan Xiong[a, b, c], Andrew B. Cundy [c], Xiaolu Guo [a, *]

[a] Key Laboratory of Advanced Civil Engineering Materials of Ministry of Education, School of Materials Science and Engineering, Tongji University, Shanghai 201804, China;

[b] School of Civil and Environmental Engineering, Changsha University of Science & Technology, Changsha 410114, China;

[c] GAU-Radioanalytical, School of Ocean and Earth Science, University of Southampton, National Oceanography Centre (Southampton), European Way, Southampton SO14 3ZH, UK

[*] Corresponding author

[a, *]Dr and Professor, Xiaolu Guo

School of Materials Science and Engineering, Tongji University,

4800 Caoan Road, Shanghai 201804, PR China.

Email address: guoxiaolu@tongji.edu.cn (X.L. Guo),

Phone: (86) 21-69582144.

Abstract:

Geopolymers are potentially useful materials for radioactive wastes stabilization or immobilization. This study explores the retention mechanisms of stable- and radioactive-Cs and Sr in fly ash (FA)/ground granulated blast furnace slag (GGBS) blended geopolymer materials by examining the evolution of phases evolution and gel structures during geopolymer curing and subsequent element/radionuclide leaching behavior in Milli Q water (MW) and simulated Sellafield underground water (UW). Results show that Cs^+ incorporation altered gel structures, while Sr^{2+} disrupted the geopolymerization process and generated $SrCO_3$. Diffusion and dissolution mechanisms governed the leaching of Cs^+ from the geopolymer, with geopolymer undergoing gel structural transformations during leaching in both MW and UW, while Cs^+ may facilitate Al release in the UW. Diffusion mechanism primarily drove the leaching of Sr^{2+} from geopolymer into Milli Q water, involving localized structural reorganization. Leaching in the UW probably involved gel transformation/reorganization and $SrCO_3$ dissolution. Cs was more mobile than Sr regardless of whether stable or radioactive nuclides were applied, and compared with conventional cement stabilisers, geopolymer exhibited better immobilization. The leaching results and immobilization mechanisms of geopolymer for stable and radioactive nuclides were not always completely aligned, warranting further direct investigation using radioactive nuclides. This study provides a perspective on product evolution both during geopolymer incorporation and subsequent leaching of Cs and Sr, and highlights the potential of geopolymer materials to effectively stabilize and immobilize Cs and Sr-containing nuclear wastes.

Keywords: Cs; Sr; fission products; geopolymer; leaching behavior; retention mechanism

1. Introduction

As many nations shift away from fossil fuel-derived power, nuclear energy is undergoing a relative renaissance, with *ca*. 85 power reactors (with a total gross capacity of about 80 GWe) planned globally, with development particularly intense in Asia [1]. For example, by 2025, there were a total of 58 nuclear power units in operation in China, with the electricity generating capacity of these nuclear power plants making up 5.08% of the nation's total electricity output [2,3]. However, the application of nuclear power inevitably generates quantities of radioactive waste which need to be effectively managed both during operation and following site shut-down and decommissioning, requiring waste treatment and packaging, storage and disposal, land remediation, decontamination and so on [4]. Within the nuclear industry, cement solidification has been one of the most predominant adopted techniques for managing intermediate and low-level radioactive wastes due to its advantages of high material strength, low cost and relative simplicity [5]. However, apart from the high energy consumption and carbon dioxide emissions during conventional cement production, there are a number of challenges posed by storage and disposal of cement solidified bodies, arising from their low densification and poor leaching resistance [6].

When considering materials for nuclear waste immobilization, geopolymers present superior alternatives to Ordinary Portland Cement (OPC). For example, the presence of water or moisture in cementitious waste forms or storage containers presents significant concerns. Interaction with ionizing radiation generated by the radioactive decay of radionuclides induces radiolysis, leading to the formation of H_2. The accumulation of H_2 will cause structural damage, including cracking of the storage matrix, and pose operational risks, as large quantities of H_2 could be released within storage facilities, potentially resulting in explosive conditions[7]. In contrast, geopolymers are generally

considered to contain lower amounts of water, although the water content of geopolymers is closely related to the precursor [8,9]. Therefore, with optimized mix design and curing conditions, geopolymers exhibit a range of benefits including reduced water content, enhanced resistance to chloride penetration, diminished leachability of radioactive ions, as well as improved thermal stability [10]. Therefore, it has been widely argued that geopolymer matrices can be used as effective immobilization materials in the disposal of intermediate and low level nuclear wastes [11]. Among relevant studies, the testing of geopolymer stabilization for nuclear material disposal can be mainly divided into two main areas. The first involves the direct incorporation and disposal of (simulated) radionuclides to understand the interaction between geopolymer and radionuclides, involving the immobilization and adsorption of (simulated) radionuclides [12]. The second involves the disposal of various forms of radionuclide-containing wastes, including sewage sludge ash contaminated with radiocesium [13], uranium-contaminated soils [14], treated radioactive solid organic waste [15] etc. In addition, geopolymer has been used to dispose of related radwastes, such as nuclear grade resins loaded with ^{134}Cs [16], high viscosity organics [17], ion exchange resins [18,19], radwaste oil [20] and liquid oil waste [21].

Cesium (Cs) and strontium (Sr) immobilization has been widely investigated [22,23]. Radioactive ^{137}Cs (half-life 30.12 years) is one of the most problematic isotopes among high-yield ^{235}U fission products due to its pronounced water solubility, high mobility, and chemical similarity to Na^+ and K^+ ions [24]. Strontium-90 (half-life 28.91 years) is also a high-yield ^{235}U fission product, with chemistry is similar to that of Ca^{2+} [25]. Studies have shown that ion exchange, physical adsorption and encapsulation are generally believed to be the main immobilization mechanisms when geopolymers are used for the immobilization of Cs^+ and Sr^{2+} [26]. Upon Cs incorporation, Cs

exhibited no significant influence on the kinetics of the geopolymerization reaction, with Cs^+ mainly bound through ion exchange into alkaline aluminosilicate gels [27–30]. Arbel-Haddad et al. [31] also reported preferential Cs incorporation into zeolite phase. Although Cs^+ and Sr^{2+} are both cations, the incorporation of Sr exhibited greater complexity. Mukiza et al. [28] showed that the presence of Sr resulted in a reduction of the geopolymerization degree of the metakaolin-based geopolymer. This occurred because the Sr^{2+} ions reacted with the OH^- ions from the alkali activator, while the effects of Sr incorporation on geopolymer reaction products and immobilization depend on its incorporation ratio. When Sr/Na$\leqslant$0.005, Sr^{2+} was found to incorporate into extra framework sites within (N,K)-A-S-H gels. At higher Sr/Na ratios, the formation of $SrCO_3$ is observed. In this case, geopolymer immobilized Sr via dual mechanisms: bind Sr within a (N,Sr,K)-A-S-H gel chemically and encapsulate excess Sr in the form of $SrCO_3$ physically [32]. The results of Walkley et al. [33] also show the incorporation of Sr^{2+} would displace some Na^+ and K^+ from charge-balancing sites, similar to the role of Ca^{2+}. The phenomenon of $Sr(OH)_2$ and $SrCO_3$ precipitation was also reported by Vandevenne et al. [29] and Mukiza et al. [28]. In terms of immobilization effects, numerical studies have indicated that the cumulative Sr fraction leached from geopolymer is lower than that in cement [34–40], even in aggressive leaching environments (such as high-temperature, freeze-thaw cycles, and acid environments). However, relatively limited studies have focused on the microstructural evolution of these products in order to understand leaching mechanisms. Komljenović et al. [41] examined the nanostructures of alkali-activated slag samples (AABFS), and suggested that the incorporation of Cs followed by leaching induced structural evolution in the AABFS nanostructure. During the leaching process, most Al was released from the C-A-S-H gel and retained within the AABFS matrix evidenced by no detected Q^2(1Al) and Q^3(1Al) sites, and

117 additionally formed Q^4(mAl) (m=1–4) sites, initiated a reconstruction of the gel phase. This
118 involved the conversion of the C-A-S-H gel to C-S-H gel and the additional formation of an N-(C)-
119 A-S-H gel. And Cs was observed to preferentially associate with the N-(C)-A-S-H gel rather than
120 with the C-A-S-H gel. This study indicates that the examination of geopolymerization products
121 before and after Cs (and Sr) incorporation, and before and after leaching, can be usefully compared
122 to obtain a better understanding of the retention mechanisms of these radionuclides in geopolymers.
123 Most studies published (and referenced above) involve use of stable nuclide simulants as
124 substitutes, rather than radioactive nuclides. However, the properties of radioactive waste water and
125 stable nuclide simulant solutions may not be exactly the same, and (in addition) shorter and medium
126 lived radionuclides will be present in much lower masses than when their stable isotopic forms are
127 used (unless very high activities, which cause issues in materials handling and disposal, are used)
128 which may lead to differences in behavior compared to stable nuclides. Additionally, while
129 immobilization mechanisms are frequently discussed, few studies have comprehensively assessed
130 the effect of nuclide incorporation (IN) and the effect of leaching (OUT), i.e., the whole process,
131 particularly from the perspective of product transformation. Therefore, in order to understand the
132 mechanisms governing Cs and Sr incorporation into geopolymers and their subsequent leaching
133 behavior, this work systematically investigates the product evolution of geopolymers before and
134 after Cs/Sr incorporation, and before and after leaching experiments through X-ray Diffraction
135 (XRD), X-ray photoelectron spectroscopy (XPS) and Solid State Magic Angle Spinning Nuclear
136 Magnetic Resonance (solid-state MAS NMR) methods. Furthermore, leaching experiments were
137 conducted not only on stable nuclides but also on geopolymer materials containing radioactive Cs
138 and Sr (specifically ^{137}Cs and ^{90}Sr) to comprehensively evaluate leaching behavior.

2. Materials and methods

2.1 Raw materials

Fly ash (FA) was supplied by the CEMEX company (UK), with less than 5 wt% CaO, which can be classified as low-calcium fly ash or Class-F fly ash. Ground granulated blast furnace slag (GGBS) was supplied by the Hanson company (Heidelberg materials, Germany). The loss of FA and GGBS on ignition at 1000 ℃ was 5.37 % and 0.12 %, respectively, according to the standard "Test Methods of Materials Stabilized with Inorganic Binders for Highway Engineering JTG 3441-2024 (T 0817–2009 The methods for measuring the loss of fly ash)"[42]. CEM II cement was supplied by TARMAC (UK) and used as a comparison matrix. $CsNO_3$ and $SrCl_2 \cdot 6H_2O$ used in this paper were supplied by Sigma-Aldrich (UK).

Table 1 Chemical composition of raw materials used in geopolymer production (wt%)

Compound（wt%）	SiO_2	Al_2O_3	CaO	Fe_2O_3	MgO	TiO_2	K_2O	Na_2O
FA	47.50	22.90	4.29	8.25	1.63	0.98	3.01	0.85
GGBS	32.80	11.10	38.30	0.44	6.64	0.60	0.55	0.31

The chemical composition of the FA and GGBS is listed in Table 1, and the mineral phases of the FA and GGBS are shown in Fig.1(a). The main phases present are quartz, mullite, and maghemite from the XRD pattern of FA. There is a broad peak between 25-35° in the XRD pattern of GGBS, with a quartz peak observed around 27°, indicating that the GGBS was predominantly amorphous. Particle size distributions were obtained using a Malvern Mastersizer 3000 based on the dry powder dispersion method (Fig.1(b)). According to the results, the particle size of FA ranged from 0.1 μm to 860 μm, with a peak at 27.37 μm. Compared with FA, the particle size range of GGBS is smaller, ranging mainly from 0.11 μm to 272.43 μm, with a peak at 18.66 μm.

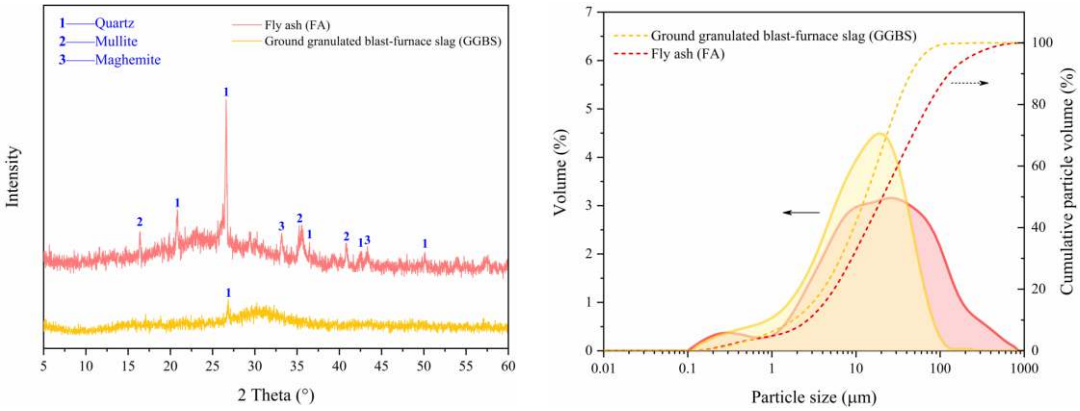

(a) XRD (b) Particle size distribution

Fig.1 Mineralogical and size characteristics of FA and GGBS

The alkali activator used in this work was composite alkali activator, prepared from water glass and NaOH 24 hours in advance of its use. The water glass used here was sourced from Chemiphase Ltd (UK), with 29.39 wt% SiO_2 and 8.99 wt% Na_2O, and a solid content of 38.38%. NaOH was sourced from Fisher Scientific (UK), with a solid content of 98.5%.

2.2 Sample preparation

2.2.1 Mix Proportion

For geopolymer samples, the mass ratio of FA to GGBS used was 7:3. The composite alkali activator used in this study was prepared with a modulus ($M = n(SiO_2)/n(Na_2O)$) of 1.4, and content of 10% (by Na_2O mass). The water-to-solid ratio of geopolymer samples was 0.4, and the water-to-cement ratio of cement for comparative samples was also 0.4.

For samples containing stable Cs and Sr, the contents of $CsNO_3$ and $SrCl_2 \cdot 6H_2O$ were set to 5 wt % of the mass of solid raw materials. It should be noted that the effect of water of crystallization in $SrCl_2 \cdot 6H_2O$ was not taken into consideration, therefore, the effective water-to-solid ratio of sample with Sr would be slightly large. When preparing samples with radioactive ^{137}Cs and ^{90}Sr, the activity was determined according to the limit of detection of each radionuclide, with specific mix

proportions shown in Table 2.

Table 2 The mix proportion of samples with stable and radioactive nuclides

Sample ID	$CsNO_3$ （wt %, by raw materials mass）	$SrCl_2 \cdot 6H_2O$ （wt %, by raw materials mass）	^{137}Cs （Bq per sample）	^{90}Sr （Bq per sample）
Geo	-	-	-	-
Cem	-	-	-	-
GeoCs5	5 wt %	-	-	-
CemCs5	5 wt %	-	-	-
GeoSr5	-	5 wt %	-	-
CemSr5	-	5 wt %	-	-
GeoCs137*	-	-	90.9 Bq	-
CemCs137	-	-	90.9 Bq	-
GeoSr90	-	-	-	18.18 Bq
CemSr90	-	-	-	18.18 Bq

*Note: The detailed mix proportion of geopolymer samples with radioactive ^{137}Cs is shown in Supplementary materials.

Milli Q water (MW) and simulated underground water (UW) (as shown in Table 3) were prepared to carry out the leaching experiments.

Table 3 Simulated underground water composition. This composition broadly simulates groundwater composition at the UK's Sellafield nuclear site, adapted from [43].

Reagent	**Concentration**
$MgSO_4$	50 mg/L
$KHCO_3$	11 mg/L
$CaCl_2.2H_2O$	143.53 mg/L
$NaHCO_3$	94 mg/L
NH_4NO_3	32 mg/L
0.1 M HCl	6 mL/L

2.2.2 Preparation methods

(1) Samples with no additional Cs and Sr

For the preparation of geopolymer samples with no additional Cs and Sr, the solid raw materials were first pre-mixed uniformly. Subsequently, a mixed solution of alkali activator and water was added, and the mixture was stirred at 140 rpm for 2 minutes using a handheld mixer (Model ID:

187 Russell Hobbs Hand Mixer 22230-56). For the preparation of cement samples with no additional
188 Cs and Sr, the basic procedure was similar to the geopolymer preparation, except that the mixed
189 solution of alkali activator and water was replaced with a specific mass of water. Geopolymer and
190 cement samples with no added Cs and Sr were named as Geo and Cem, respectively.

191 **(2) Samples with stable nuclides**

192 When preparing geopolymer samples with Cs, the required mass of $CsNO_3$ solid powder was
193 evenly mixed with the solid raw materials, and then the same preparation process as that of the
194 geopolymer with no added Cs and Sr was followed. When preparing geopolymer samples with Sr,
195 $SrCl_2 \cdot 6H_2O$ was dissolved in excess water initially, then the solid materials and alkali activator were
196 mixed for 2 mins. Finally, the dissolved solution was added into the fresh pastes, mixing for another
197 2 mins.

198 For cement samples with Cs, $CsNO_3$ solid powders were mixed with cement powders for 2
199 mins initially, and then mixed with water for another 2 mins. When preparing cement samples with
200 Sr, $SrCl_2 \cdot 6H_2O$ was initially dissolved with 1/5 of the mass of the water. Then cement was mixed
201 with the other 4/5 of the mass of the water for 2 mins, then mixed with $SrCl_2 \cdot 6H_2O$ solution for
202 another 2 mins.

203 **(3) Samples with radioactive nuclides**

204 For the preparation of geopolymer with ^{137}Cs and ^{90}Sr, solid raw materials were first premixed
205 uniformly, and then alkali activator was added and mixed for 2 mins to form a fresh paste. The
206 calculated mass of water was divided into two portions. A half mass of Milli Q water was initially
207 used to prepare the radioactive nuclide solution (containing (a) ^{137}Cs with an initial activity of 2.183
208 kBq/g, in 0.1M HCl with 100 μg/ml Cs carrier (AEA Technology QSA, UK), and (b) ^{90}Sr with an

initial activity of 1.468 kBq/g, in 0.1M HCl with 30 mg/ml Sr carrier (PTB, Germany)) in a plastic bottle, which was subsequently incorporated into the fresh paste and thoroughly mixed for 1 min via manual stirring using a wooden stick. The remaining water was then used to rinse residual radioactive nuclide solution from the plastic bottle, with this rinse water also being added to the paste followed by an additional 1 min of manual stirring.

For the preparation of cement with ^{137}Cs and ^{90}Sr, the calculated mass of water was divided into three portions. At first, cement and 4/5 mass of water were mixed for 2 mins to prepare a fresh paste. Then 1/10 mass of water was used to prepare the radioactive nuclide solution, which was subsequently incorporated into the fresh paste and thoroughly mixed for 1 min via manual stirring using a wooden stick. Similarly, the remaining water was then used to rinse residual radioactive nuclide solution from the plastic bottle, with this rinse water also being added to the paste followed by an additional 1 min of manual stirring.

2.3 Leaching experiments

To investigate stability of cement and geopolymer samples containing stable and radioactive nuclides, leaching experiments were implemented according to the national standard “Standard test method for leachability of low and intermediate level solidified radioactive waste forms (GB/T 7023-2011)”. Milli Q water and Sellafield simulated ground (underground) water were used as leachants. When the leachate is Milli Q water, the suffix of the sample ID is ‘MW’, and when the leachate is simulated underground water, the suffix of the sample ID is ‘UW’. Samples used for the leaching experiments were cylindrical samples with a diameter of 24 mm and a height of 25 mm after ambient curing for 28 days. The samples were tied with fine nylon ropes so that they could be suspended in the leachant (See Fig.2), and the leachant volume used was 400 mL. For samples with

stable nuclides, the leachate was replaced on the 1 st, 3 rd, 7 th, 10 th, 14 th, 21 st, 28 th, 35 th, and 42 nd days from the begin of the leaching test, then collecting the leachate and measuring the Cs and Sr ion concentration. For samples with radioactive nuclides, a short-term leaching test was carried out and the effect of decay was not considered.

The leaching rate and cumulative fraction leached (CFL) of nuclides were calculated according to Eq. (1) and (2):

$$R_n = \frac{a_n/A_0}{(S/V)(\Delta t)_n} \quad (1)$$

$$CFL = \frac{\sum a_n/A_0}{S/V} \quad (2)$$

where R_n represents the leaching rate of the component during the nth leaching cycle (cm/d); a_n represents the activity or mass of the component leached during the nth leaching cycle (Bq or g); A_0 represents the initial activity or mass of the component in Cs/Sr-containing sample (Bq or g); S represents the geometric surface area of the sample in contact with the leachant (cm^2); V represents the volume of the sample (cm^3); $(\Delta t)_n$ represents the duration of the nth leaching cycle (d), $(\Delta t)_n = t_n - t_{n-1}$; CFL represents cumulative fraction leached of the component at the time t (cm); t represents the cumulative leaching time (d), $t = \sum(\Delta t)_n$.

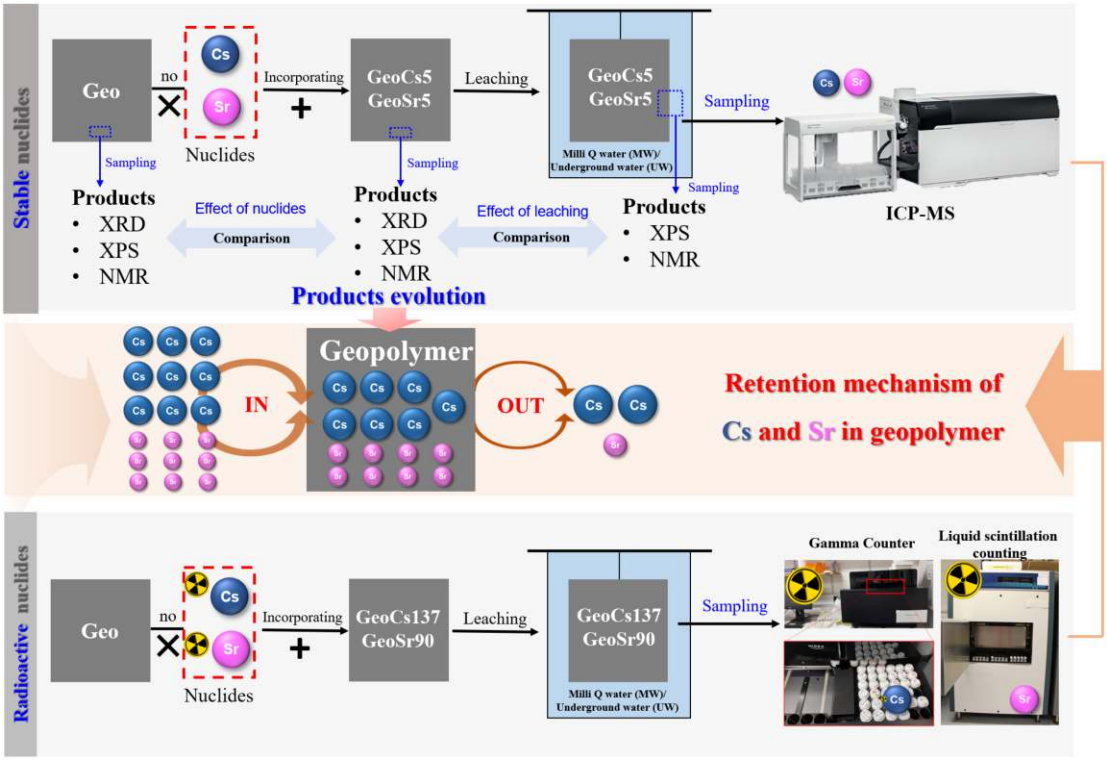

Fig.2 Summary of experimental program

After leaching tests, the experimental results was fitted to different mathematical models, which is representing different leaching mechanisms [44]. During our preliminary data processing, the correlation coefficient using a first-order reaction model was negative, indicating that leaching behaviors of Cs and Sr are not controlled by a first-order reaction. Therefore, in subsequent discussions, the first-order reaction model was not considered. Mathematical models including the **diffusion model (DFM), dissolution model (DSM) and** their **combination model** were used for fitting and are presented as follows:

(1) Diffusion model (DFM)

When the transport of nuclides is governed by diffusion, the flux of the diffusing materials $J(t)$ through the immobilized matrix can be determined by the solution of Fick's second law in semi-infinite medium and Fick's first law as Eq. (3):

$$J(t) = -D\frac{\partial C}{\partial x}\Big|_{x=0} = -C_0\sqrt{\frac{D}{\pi t}} \quad (3)$$

where C_0 represents the initial concentration in the immobilized matrix and D represents the diffusion coefficient. The leached activity or mass from a unit surface area during time $A_n(t)$ is expressed as Eq. (4).

$$A_n(t) = \int_0^t J(t)dt = 2A_0\sqrt{\frac{Dt}{\pi}} \quad (4)$$

Therefore, the cumulative fraction leached from the immobilized matrix can be described as Eq.(5).

$$\frac{\sum A_n}{A_0} = 2\left(\frac{S}{V}\right)\sqrt{\frac{Dt}{\pi}} \quad (5)$$

where $\sum A_n$ is the cumulative amount leached during cumulative time.

(2) Dissolution model (DSM)

When a structurally major component is leached from the waste form, the matrix's integrity would break down, a process known as dissolution. The dissolution kinetics can be described by a network dissolution velocity U, which is defined as the volume of solid material being dissolved per unit time and per unit surface area of solid exposed:

$$U(t) = U_0\left(1 - \frac{C^w(t)}{C^w_{sat}}\right) \quad (6)$$

where U_0 is the maximum network dissolution velocity and C^w_{sat} is the saturation concentration in the aqueous solution. For the simple case where $C^w_{sat} >> C^w(t)$, $U(t)$=U_0, and the cumulative fraction leached (CFL) could be expressed as Eq. (7).

$$CFL = \frac{S}{V}U_0 t \quad (7)$$

(3) Combination model

The combination model assumes that diffusion and dissolution drive the leaching process, with a combined diffusion and dissolution model as Eq. (8).

$$CFL = 2\left(\frac{S}{V}\right)\sqrt{\frac{Dt}{\pi}} + \frac{S}{V}Ut \quad (8)$$

2.4 Testing methods

The concentration of stable nuclides in the leachate was determined via Inductively Coupled Plasma Mass Spectrometry (ICP-MS), using an Agilent 8880 ICP/MS/MS system (sample workflow and analysis is illustrated in Fig.2). Radionuclide activity measurements were conducted at the GAU-Radioanalytical Laboratories at the National Oceanography Centre (Southampton), University of Southampton, UK. The activity of ^{137}Cs was measured using a Hidex gamma counter, while the activity of ^{90}Sr was measured via Cerenkov counting using a liquid scintillation counter, model Quantulus 1220, with a counting time of 24 hours.

The XRD spectra of the geopolymer after 28 d curing were determined using a Philips X'Pert Pro with Cu-Kα radiation, with a scanning speed of 0.4 °/min and a scanning range of 5°~60°. Dried geopolymer powder samples were also measured via X-ray photoelectron spectroscopy (XPS, S8 Tiger) using Al Kα X-ray source and the flood gun was opened to give charge compensation. The high resolution spectra were measured with a pass energy of 30 eV. For the XPS analysis of samples after leaching tests, the sampling location was the sample portion in contact with the leachant. Spectra were analyzed using Thermo Advantage software and have been charge corrected to main line of the carbon C1s set to 284.80 eV.

A solid-state ^{29}Si Dipole decoupling magic angle spinning (DD/MAS) experiment was performed using an Agilent 600 DD2 spectrometer (Agilent, USA, magnetic field strength 14.1T) with a Larmor frequency of 199.13 MHz for ^{29}Si and proton decoupling (TPPM) during acquisition. The powder samples were placed in a pencil-type zirconia rotor of 4.0mm. The spectra were obtained at a spinning speed of 8 kHz with a recycle delay of 3 s, an approximately 90-degree pulse (4 us) and 1024 scans. The Si signal of tetramethylsilane (TMS) at 0 ppm was

used as the reference for the ^{29}Si chemical shift. For the MAS NMR analysis of samples after leaching tests, the sampling location was the portion in contact with the leachate. For ^{27}Al DD/MAS NMR Measurements, experiments were carried out on the same instrument with a Larmor frequency of 156.25 MHz for ^{27}Al and proton decoupling (TPPM) during acquisition. As previously, the powder samples were placed in a pencil-type zirconia rotor of 4.0 mm. The spectra were obtained at a spinning speed of 8 kHz with a recycle delay of 1s, an approximately 90-degree pulse (3.6 us) and 128 scans. The Al signal of $AlCl_3$ at 0.9 ppm was used as the reference of ^{27}Al chemical shift. Subsequent peak fitting and deconvolution were performed using PeakFit software. The assignments of deconvoluted peaks and applying Gaussian functions were determined according to the literatures [45,46]. The FWHM was kept consistent and maintained below 10 ppm [41].

It should be noted that the tests of products and structures involved stable nuclides rather than high activities of radioactive nuclides in order to avoid environmental and experimental risks. Radioactive nuclides were only assessed in the leaching experiments.

3. Results and discussions

3.1 The impact of incorporated Cs on geopolymer structure

Fig.3 illustrates XRD patterns of geopolymer containing stable Cs. The sample without Cs incorporation (Geo) contained quartz and mullite, which originated from unreacted fly ash, along with calcite. The co-existence of geopolymer gel and calcium silicate hydrate gel was indicated by the presence of C-(A)-S-H [47] and a prominent amorphous feature (25°~35°). With the incorporation of Cs, these main phases remained the same.

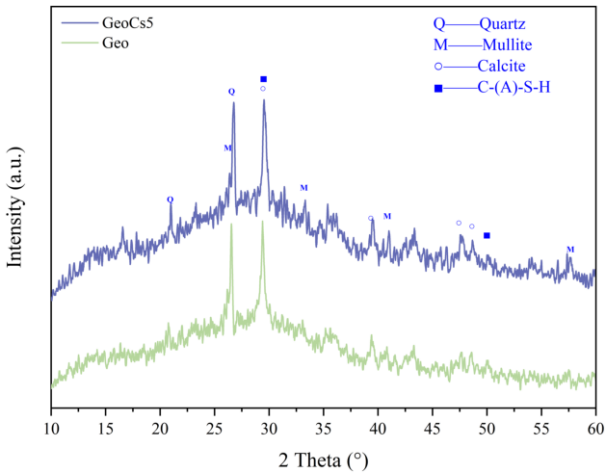

Fig.3 The XRD patterns of geopolymer samples with and without added Cs

Fig.4 presents XPS spectra for geopolymer samples with and without Cs. From the Cs 3d spectrum of GeoCs5 (Fig.4(a)), two peaks were observed near 738.64 eV and 724.64 eV, corresponding to Cs 3d. From the Al 2p spectrum (Fig. 4(b)), in addition to the main peak near 74.00 eV, peaks were also observed near binding energies of 75.57 eV and 77.84 eV, which represents overlapping peaks of Cs 4d according to related studies [48]. From the Si 2p spectrum (Fig. 4(c)), with the incorporation of Cs, the binding energy of Si 2p slightly increased, from 102.24 eV to 102.34 eV. Compared with Na^{+} and Ca^{2+}, the ionic radius of Cs^{+} is larger and its electronegativity is lower. When Cs is incorporated, it would fulfil a charge-balancing role (by occupying Na^{+} and/or Ca^{2+}), resulting in weaker shielding of Si and consequent increased Si binding energy.

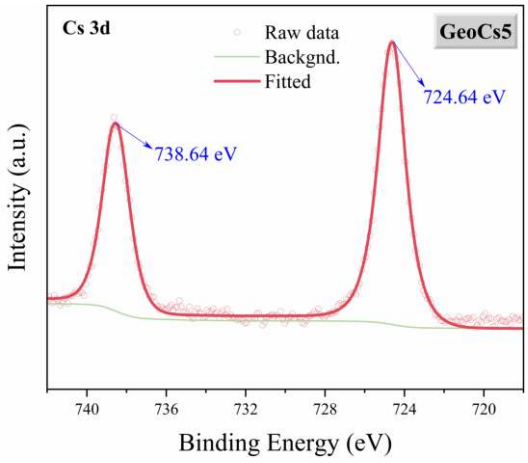

(a) Cs 3d

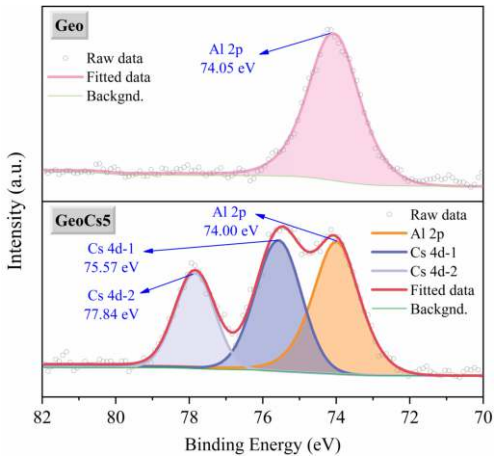

(b) Al 2p (and Cs 4d)

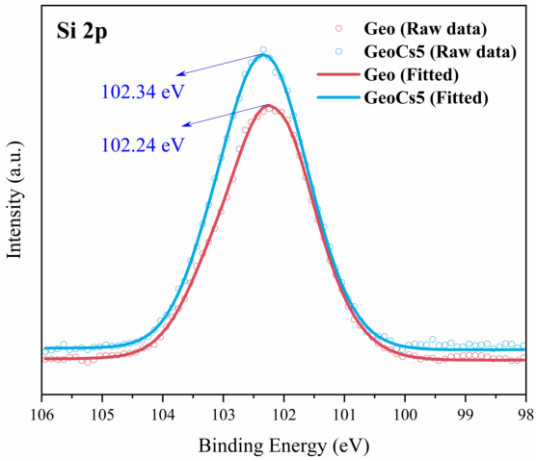

(c) Si 2p

Fig.4 The effect of Cs incorporation on the binding energy of the geopolymer

However, conventional powder XRD methods have limited capability for the quantitative structural analysis of geopolymer gels due to their low crystallinity. For phases exhibiting such limited long-range order, the solid-state magic angle spinning nuclear magnetic resonance (MAS NMR) is a superior method to elucidate details of the local structure. Therefore, to understand the impact of Cs incorporation on the molecular structures of geopolymer, solid-state MAS NMR analysis was performed on geopolymer samples with and without Cs. Fig.5 illustrates ^{27}Al MAS NMR spectra of geopolymer samples with and without Cs incorporation. For the geopolymer sample without Cs, the resonance peaks primarily appear at chemical shifts of 61.05 ppm and 9.17 ppm. Based on the descriptions of chemical shifts for different Al sites [49,50], the main peak of the ^{27}Al spectrum near 61 ppm represents tetrahedral coordination, and the peak of the ^{27}Al spectrum near 10 ppm represents octahedral coordination. The study by Bernal et al. [51] also identified a sharp signal at 5 ppm in alkali-activated FA/GGBS blends, which is attributed the presence of Al(VI) in nanostructured octahedral environments, potentially resembling the third aluminate hydrate phase, hydrotalcite and/or katoite. With Cs incorporation, the peaks of the ^{27}Al spectrum for the GeoCs5 sample shifts (from 61.05 ppm to 60.45 ppm, from 9.17 ppm to 5.81 ppm), suggesting that the

incorporation of Cs affects the local environment of Al in the geopolymer, while the spectral shape and relative intensity remain unchanged, indicating that the primary structure of the geopolymer is not significantly altered.

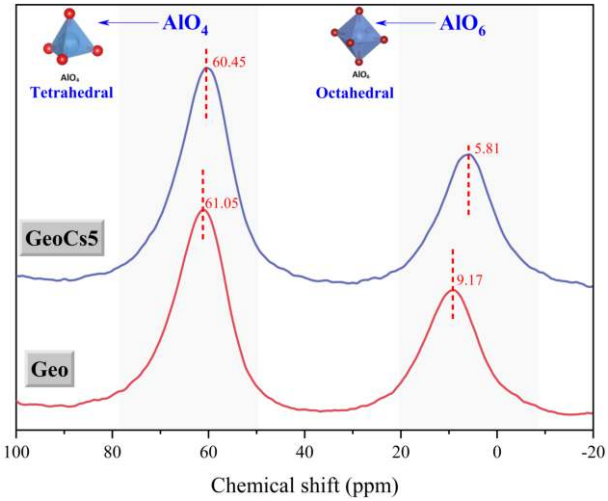

Fig.5 The ^{27}Al spectra of geopolymer samples with and without Cs

The ^{29}Si MAS NMR spectra were deconvolved and analyzed as shown in Fig.6. The chemical environments of ^{29}Si are denoted by Q^n [50], where *n* (ranging from 0 to 4) is the number of bridging oxygen atoms, which connects a silicon tetrahedron to neighboring silicon tetrahedra. Q^0 corresponds to isolated [SiO_4] tetrahedra; Q^1 represents silicon tetrahedra that share one oxygen atom with another silicon tetrahedron, forming short chains, typically found at the ends of dimers or polymer chains; Q^2 denotes silicon tetrahedra that share two oxygen atoms with two neighboring silicon tetrahedra, forming longer chains or ring structures; Q^3 refers to silicon tetrahedra that share three oxygen atoms with three neighboring silicon tetrahedra, forming branched or cross-linked chain or layered structures; and Q^4 represents silicon tetrahedra connected to four neighboring silicon tetrahedra, forming a three-dimensional network structure. The m in Q^n(mAl) ($m \leqslant n$) specie denotes the number of aluminum neighbors. The ^{29}Si MAS NMR spectra of the geopolymer were deconvolved and analyzed, with the deconvolution fitting results presented in Fig.6 and Table 4 (last

page).

Fig. 6 (a) demonstrates the effect of Cs incorporation on the ^{29}Si MAS NMR spectra of the geopolymer, followed by their deconvoluted spectra presented in Fig. 6(b) and Fig. 6(c), with the statistical results shown in Fig.6 (d). According to the XRD results, the geopolymerization products were the co-existence of geopolymer gel and calcium silicate hydrate gel. The resonance of C-(N)-A-S-H gel in the ^{29}Si MAS NMR spectrum ranged from -70 ppm to -90 ppm and is centered at around -85 ppm, and the resonance of N-A-S-H gel ranged from -90 ppm to -130 ppm and is centered at around -110 ppm [50–52]. The above ^{29}Si MAS NMR analysis confirms the coexistence of C-(N)-A-S-H and N-A-S-H gel, which aligns with the XRD results (above). As shown in Fig. 6(d), the incorporation of Cs leads to an increase in the relative content of Q^1 units, indicating that Cs introduction affects the overall network structure. Besides, the relative content of Q^4(0Al) increased with Cs incorporation, suggesting that the Cs incorporation may affect the dissolution of raw materials. Mukiza et al. [28] also observed that the Cs addition led to a slight reduction of the first sharp and narrow heat release peak associated with the wetting and dissolution of precursor appeared in less than 10 min, although they found that the addition of $CsNO_3$ exerted no significant influence on the cumulative heat evolution during geopolymerization. Compared with the no-Cs geopolymer sample, the Cs-containing geopolymer exhibits decreased relative contents of Q^3(1Al) and Q^4(3Al) units, while showing increased proportions of Q^4(2Al) and Q^4(1Al) units. In geopolymers, monovalent sodium ions (Na^+) and divalent calcium ions (Ca^{2+}) typically serve to charge-balance Al sites [53]. Q^4(3Al) represents silicon tetrahedra connected to 3 neighboring aluminum tetrahedra, necessitating 3 cations for charge balance theoretically. Considering that the aqueous ionic radius of monovalent cesium ions (Cs^+, 169 pm) significantly exceeds those of Na^+

(98 pm) and Ca^{2+} (103 pm) [54], the space of Q^4(3Al) may be insufficient to accommodate multiple Cs^+. Therefore, we suggest that Cs^+ ions are more likely to preferentially occupy more open Q^4(2Al) and Q^4(1Al) structural units for charge balancing, suggesting a potential tendency for the formation of (N,Cs)-A-S-H gel when Cs is incorporated [55]. Similarly, due to the greater ionic radius of Cs^+, the presence of Cs^+ may cause replacement of the surface cations of C-(N)-A-S-H gel, rather than the interlayer ions [56,57]. The more pronounced shift of 6-coordinated Al sites in Fig.5 may also support that Cs^+ ions may tend to occupy the interlayer or surface sites to balance charges. Further integrating experiments (e.g., X-ray absorption near edge structure spectra [58], ^{133}Cs MAS NMR [31]) and simulation methods [58] could provide direct evidence of the Cs^+ binding sites in geopolymers.

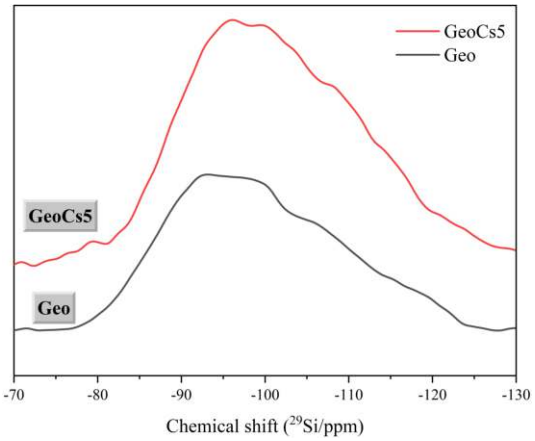

(a) ^{29}Si spectra of Geo and GeoCs5

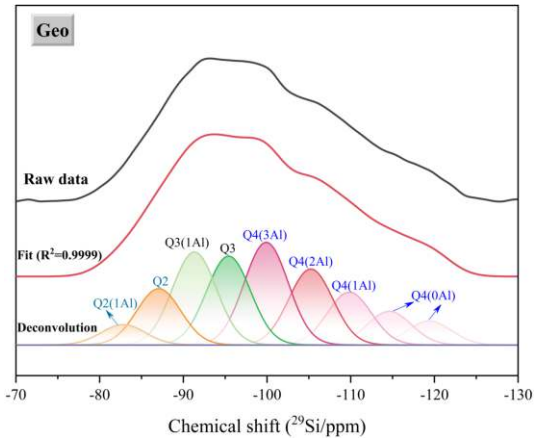

(b) Deconvolved spectra of Geo

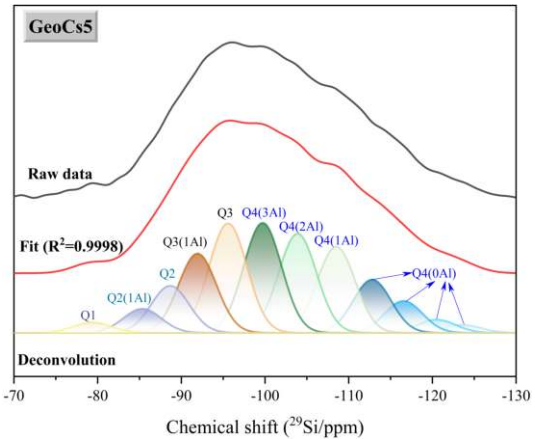

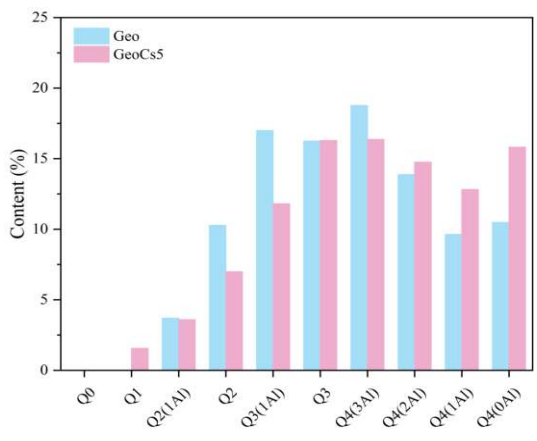

(c) Deconvolved spectra of GeoCs5 (d) Statistical results from deconvolved spectra

Fig.6 The effect of Cs incorporation on the ^{29}Si MAS NMR spectra and deconvolution results of geopolymer samples

Additionally, the bridging oxygen values (RBO) of the samples were calculated using Eq. (9) [59] as shown in Table 4 (last page).The calculated RBO value of Geo was 84.70%, while that of GeoCs5 was 86.51%, suggesting that Cs incorporation may not significantly affect the overall degree of polymerization of the structure.

$$RBO = \frac{1}{4}\left(1 \times \frac{Q^1}{\sum Q^n} + 2 \times \frac{Q^2}{\sum Q^n} + 3 \times \frac{Q^3}{\sum Q^n} + 4 \times \frac{Q^4}{\sum Q^n}\right) = \frac{1}{4}\frac{\sum n \cdot Q^n}{\sum Q^n} \quad (9)$$

Based on the above results, upon incorporation of Cs no significant changes in the main phases present can be detected from XRD results. From the XPS and MAS NMR results, the Cs incorporation altered the local environment of Al, and the larger Cs ionic radius may suggest a potential tendency for the formation of (N,Cs)-A-S-H when Cs is incorporated.

3.2 The leaching behaviors of stable and radioactive Cs-containing samples

3.2.1 Samples with stable Cs

The leaching rate and CFL of stable Cs from geopolymer and cement samples over different leaching periods is shown in Fig.7. During the initial leaching stage (<7 days), the leaching rate exhibited a progressive decline with increasing leaching time. When the leaching period exceeds 21 d, the leaching rate of Cs^+ effectively reaches a dynamic equilibrium. According to Fig.7, the Cs^+ leaching rate of geopolymer is much lower than that of cement, with the leaching rate of the samples in simulated underground water being slightly higher than that in Milli Q water. One possible reason for this phenomenon may be that competitive abundant ions in simulated underground water occupy

binding sites in the geopolymer, leading to enhanced Cs leaching rates. When the leaching period reached 42 d, the cumulative fraction leached from samples GeoCs5 and CemCs5 in Milli Q water were 0.06639 cm and 0.27137 cm, respectively, and the cumulative fraction leached from samples GeoCs5 and CemCs5 in simulated underground water were 0.07163 cm and 0.26675 cm. Compared with cement samples containing Cs (CemCs5), the cumulative Cs^+ fraction leached by Milli Q water and simulated underground water in geopolymer samples decreased by 75.5% and 73.1%, respectively. This indicates that the geopolymer exhibited a better Cs immobilization effect than cement.

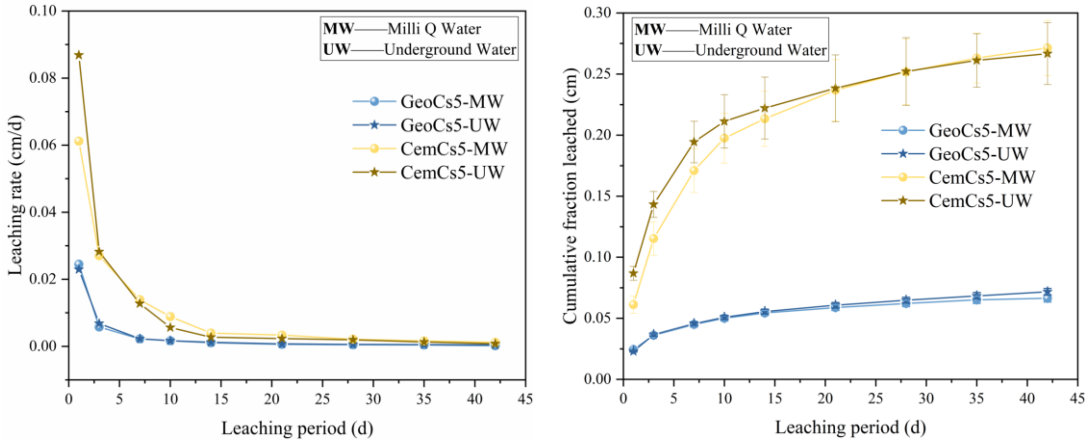

(a) Leaching rate (b) Cumulative fraction leached (CFL)

Fig.7 The leaching rate and cumulative fraction leached of samples containing Cs

The leaching data shown in Fig.7 were fitted with different mathematical models based on Eq. (3)~(8), which are shown in Fig.8 and Table 5.

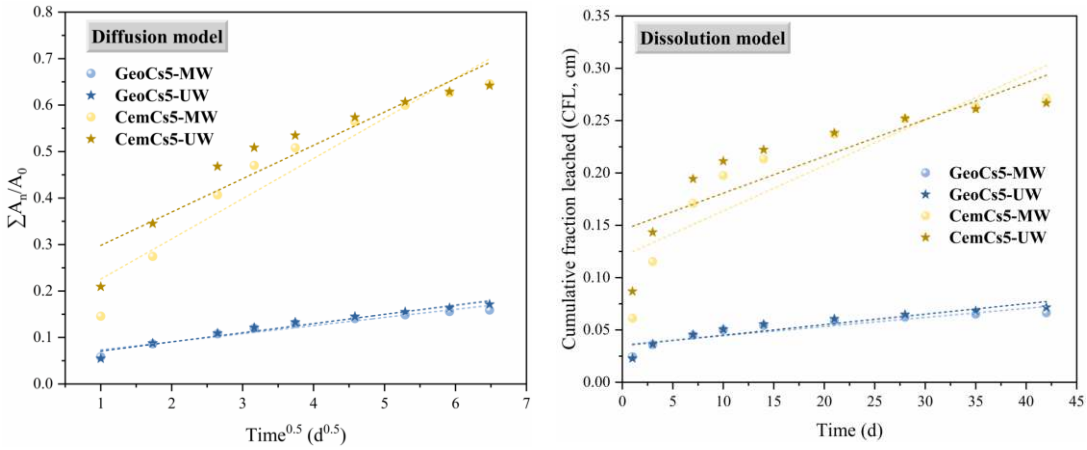

(a) Diffusion model (b) Dissolution model

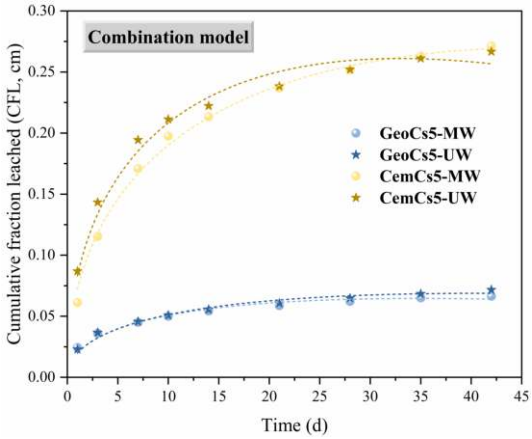

(c) Combination model

424 Fig.8 Fitting of samples containing Cs by diffusion model, dissolution model and combination model.

425

426 Table 5 R^2 of samples containing Cs fitted by leaching models

Sample ID	DFM		DSM		DFM+DSM
	D (cm^2/s)	R^2	U (cm^2/d)	R^2	R^2
GeoCs5-MW	4.80E-10	0.9328	0.000366	0.7872	0.9620
GeoCs5-UW	6.19E-10	0.9497	0.000418	0.8203	0.9718
CemCs5-MW	1.20E-08	0.9116	0.001823	0.7532	0.9937
CemCs5-UW	8.08E-09	0.8711	0.001462	0.6987	0.9778

427 As can be observed from the correlation coefficients in Table 5 for sample GeoCs5, regardless

428 of whether leaching took place in Milli Q water (MW) or simulated underground water (UW), the

429 order of the R^2 value of the leaching models is: dissolution model (DSM)<diffusion model

430 (DFM)<combined model (DFM+DSM). This indicates that the leaching mechanism of GeoCs5

431 involved both diffusion and dissolution, with diffusion primarily controlling the leaching behavior.

432 For the cement sample (CemCs5), the leaching mechanism of Cs was fundamentally the same as

433 that in the geopolymer solidified forms. For stable Cs-containing geopolymers, according to the

434 fitting results, the diffusion coefficients obtained from the diffusion model in Milli Q water (MW)

435 and simulated underground water (UW) are 4.80E-10 cm^2/s and 6.19E-10 cm^2/s, respectively, and

436 the dissolution rates obtained from the dissolution model in MW and UW are 0.000366 cm^2/d and

0.000418 cm^2/d, respectively. From these results, it can be concluded that both the diffusion coefficient and the dissolution rate of the geopolymer containing stable Cs in simulated underground water are greater than those in Milli Q water.

3.2.2 Samples with radioactive ^{137}Cs

The leaching rates and CFL of samples with radioactive ^{137}Cs are presented in Fig. 9. During the initial stage of the leaching tests, the leaching rates of all samples were relatively high, with the leaching rate of the cement samples consistently exceeding that of the geopolymer samples.

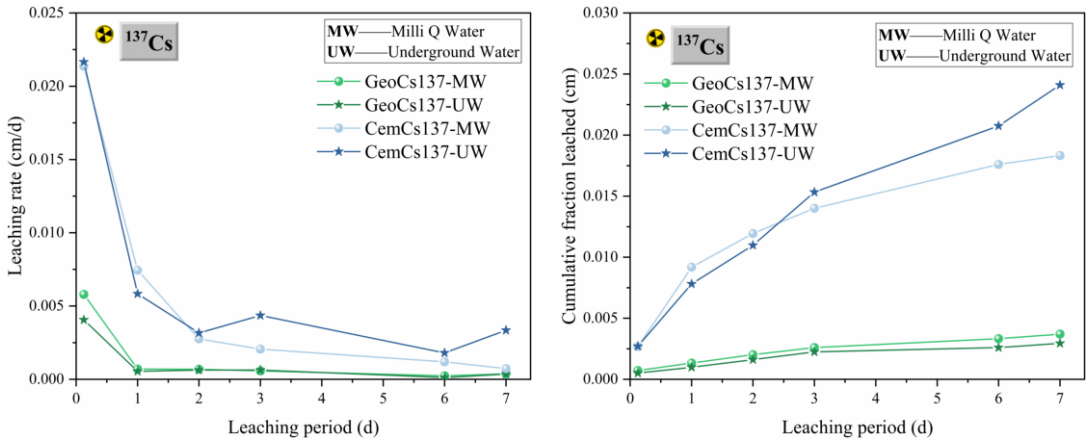

(a) Leaching rate (b) Cumulative fraction leached (CFL)

Fig.9 The leaching rate (a) and cumulative fraction leached (b) of samples containing ^{137}Cs

The same model fitting method as applied above was applied to the radioactive leaching data, and results are presented in Fig.10 and Table 6.

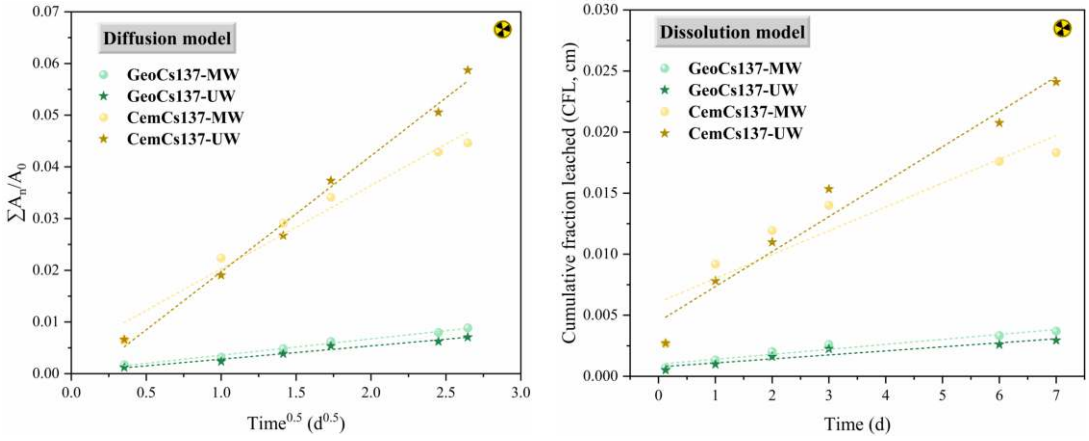

(a) Diffusion model (b) Dissolution model

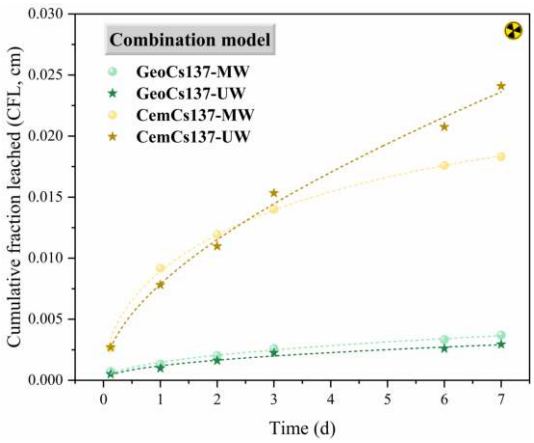

(c) Combination model

Fig.10 Fitting results of samples containing radioactive ^{137}Cs with the diffusion model, dissolution model and combination model

According to the fitting results in Table 6, for geopolymer solidified forms containing radioactive ^{137}Cs, i.e., GeoCs137, the leaching mechanism in Milli Q water was primarily dominated by diffusion, while the leaching behavior in simulated underground water was better described by a combined model of diffusion and dissolution, as indicated by a slightly higher correlation coefficient. For radioactive ^{137}Cs-containing geopolymers, according to the fitting results, the diffusion coefficients obtained from the diffusion model in Milli Q water (MW) and simulated underground water (UW) are 1.57E-11 cm^2/s and 1.06E-11 cm^2/s, respectively, and the dissolution rates obtained from the dissolution model in MW and UW are 0.000170 cm^2/d and 0.000137 cm^2/d, respectively. From these results, it can be concluded that both the diffusion coefficient and the dissolution rate of the geopolymer in Milli Q water are even slightly greater than those in simulated underground water, which is not completely aligned with the conclusion obtained from samples with stable nuclides. Levchuk et al. [60] also observed divergent results between radionuclides (^{137}Cs and ^{90}Sr) and their stable isotopes when measuring their transfer factor in soil. Therefore, the immobilization mechanism of ^{137}Cs in geopolymer requires further investigations by incorporating radioactive isotopes rather than radioactive simulants. For cement solidified forms containing radioactive ^{137}Cs,

i.e., CemCs137, regardless of whether the leachant was Milli Q water or simulated underground water, the combined model of diffusion and dissolution provided a better description of the leaching behavior, as evidenced by the higher correlation coefficients.

Table 6 R^2 of samples containing radioactive ^{137}Cs fitted by leaching models.

Sample ID	DFM		DSM		DFM+DSM
	D (cm^2/s)	R^2	U (cm^2/d)	R^2	R^2
GeoCs137-MW	1.57E-11	0.9890	0.000170	0.9374	0.9852
GeoCs137-UW	1.06E-11	0.9623	0.000137	0.8851	0.9639
CemCs137-MW	3.97E-10	0.9633	0.000800	0.8172	0.9952
CemCs137-UW	7.71E-10	0.9895	0.001174	0.9557	0.9925

3.3 The effect of leaching on the structural evolution of Cs-containing geopolymer

High-resolution X-ray photoelectron spectroscopy (XPS) was also carried out to examine the structures of geopolymer after leaching. Fig.11 presents XPS spectra of Cs 3d, Si 2p, and Al 2p for geopolymer solidified forms with stable Cs after leaching. As shown in Fig.11, the binding energies of the Cs 3d, Si 2p, and Al 2p peaks shifted toward higher values after the leaching tests, while the leachant had a minimal influence on the positions of these binding energy peaks. During the leaching process, the accompanying leaching of cations (Cs^+ and potential Na^+, Ca^{2+}) leads to a reduced shielding effect on the framework, resulting in an increase in the binding energy of Si 2p and Al 2p.

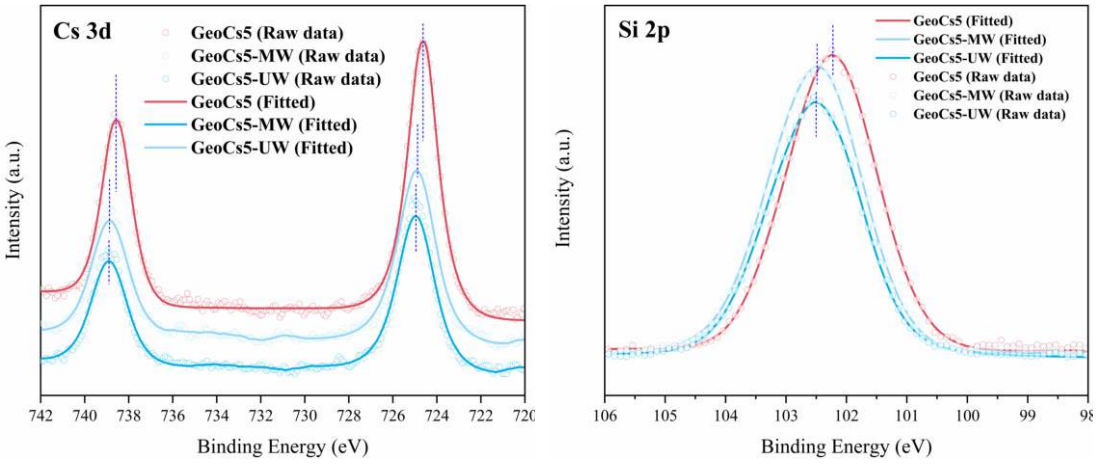

(a) Cs 3d (b) Si 2p

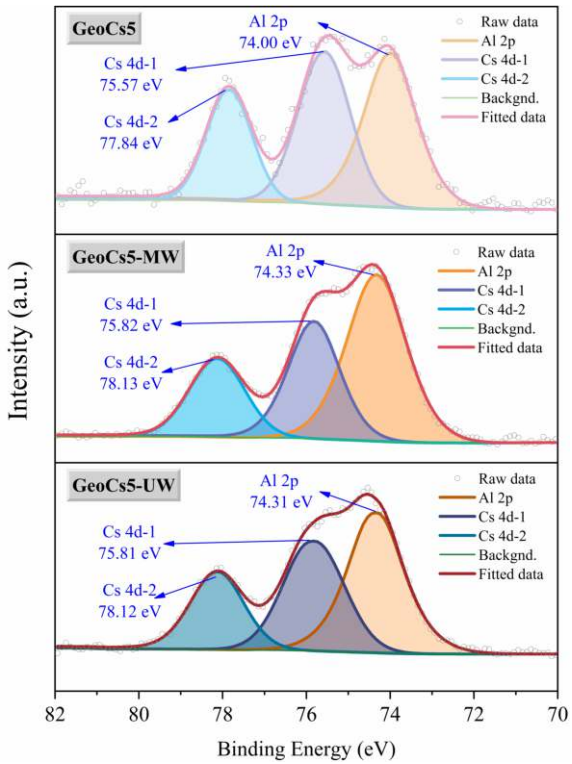

(c) Al 2p (and Cs 4d)

Fig.11 The XPS spectra of geopolymer samples with Cs before and after leaching experiments

To further clarify the molecular structural evolution of the geopolymer solidified form with stable Cs after leaching experiments, ^{29}Si MAS NMR spectroscopy was conducted on geopolymer samples subjected to leaching tests in Milli Q water and simulated underground water, as illustrated in Fig.12.

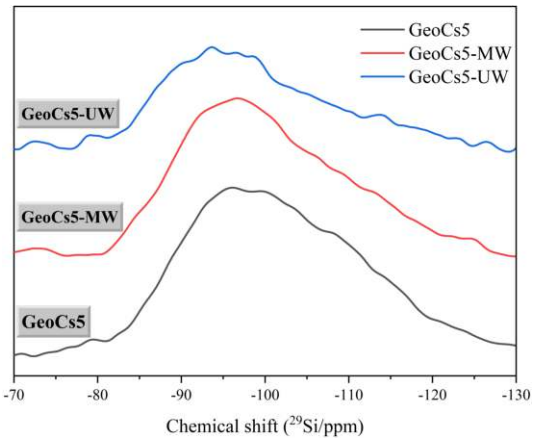

(a) ^{29}Si MAS NMR spectra of Cs-containing geopolymer before and after leaching

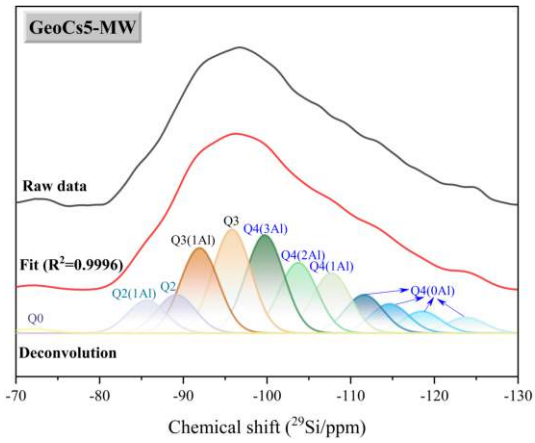

(b) deconvolved spectra of Cs-containing geopolymer after leaching in MW

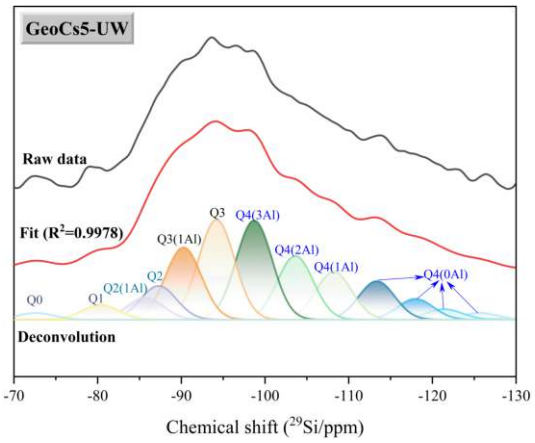

(c) deconvolved spectra of Cs-containing geopolymer after leaching in UW

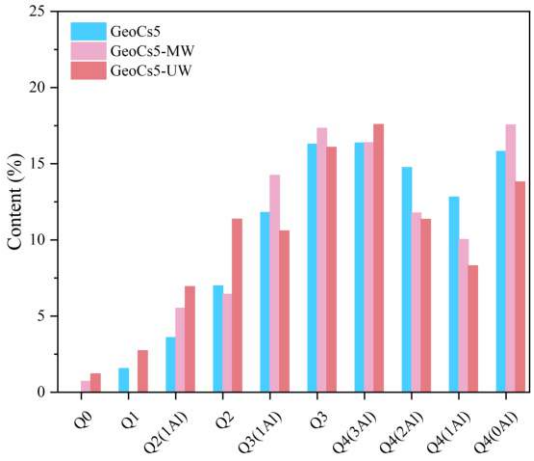

(d) the statistical results from above deconvolved spectra

Fig.12 The effect of leaching on the ^{29}Si MAS NMR spectra of geopolymer samples

Fig. 12(a) presents the ^{29}Si MAS NMR spectra of samples before and after leaching in MW (Milli Q water) and UW (simulated underground water), with their corresponding deconvolved spectra displayed in Fig. 12(b) and Fig. 12(c). The relative contents of structural units derived from deconvolved spectra are summarized in Fig. 12(d).

$$Si/_{Al}(NASH) = \frac{\sum_{n=0}^{4} Q^4\ (nAl)}{\sum_{n=0}^{4} \frac{n}{4} Q^4\ (nAl)} \tag{10}$$

$$Si/_{Al}(C(N)ASH) = \frac{Q^1 + Q^2 + Q^2(1Al) + Q^3 + Q^3(1Al)}{Q^3\ (1Al)} \tag{11}$$

$$MCL_{NC} = \frac{2[Q^1 + 3Q2(1Al) + Q^2]}{Q1} \tag{12}$$

$$MCL_C = \frac{4[Q^1 + Q^2(1Al) + Q^2 + Q^3 + 2Q^3(1Al)]}{Q1} \tag{13}$$

As shown in Fig. 12(a), the MAS NMR spectra of geopolymer sample after leaching in simulated underground water exhibit sharper profiles compared to those after leaching in Milli Q water. Fig. 12(d) reveals the emergence of Q^0 units (isolated [SiO_4] tetrahedra) after leaching, suggesting partial structural disintegration during the leaching process, consistent with previous fitting results. Eq.(10) to Eq.(13) were used to calculate the Si/Al ratio of gels and main chain length

(MCL) to understand the structural evolution during the leaching process and results are listed in Table 4. Both Q^4(2Al) and Q^4(1Al) units demonstrate reduced relative contents, while the presence of Q^2(1Al) implies potential structural rearrangement in the Cs-containing geopolymer sample. Compared to the sample leached in MW (GeoCs5-MW), the sample leached in UW (GeoCs5-UW) exhibited more pronounced increases in Q^0, Q^1, and Q^2 units, along with greater reductions in Q^4(2Al) and Q^4(1Al) units, and an increase in Si/Al ratio of C-(N)-A-S-H (Table 4), indicating C-(N)-A-S-H gel may tend to transform and reconstruct with Al release when leached in simulated underground water. The calculated cross-linked main chain length (MCL_C) results according to Eq.(13) further corroborate this observation: the sample after leaching in UW show decreased cross-linked chain lengths, also evidencing probable dissolution behavior, which is also consistent with the higher dissolution rate fitted by the leaching models when leached in simulated underground water.

3.4 The impact of incorporated Sr on geopolymer structure

Fig.13 shows the XRD patterns of geopolymer solidified forms containing stable Sr. The main phases of the geopolymer products remain the co-existence of geopolymer gel and calcium silicate hydrate gel. From the relative intensity of peaks between unreacted material (~27°) and products (~29°), which represents unreacted material and reaction products, respectively, the amount of product decreased upon incorporation of Sr compared with the geopolymer sample that did not contain Sr. Additionally, a diffraction peak observed near 25° in sample GeoSr5 may suggest the formed strontium carbonate ($SrCO_3$).

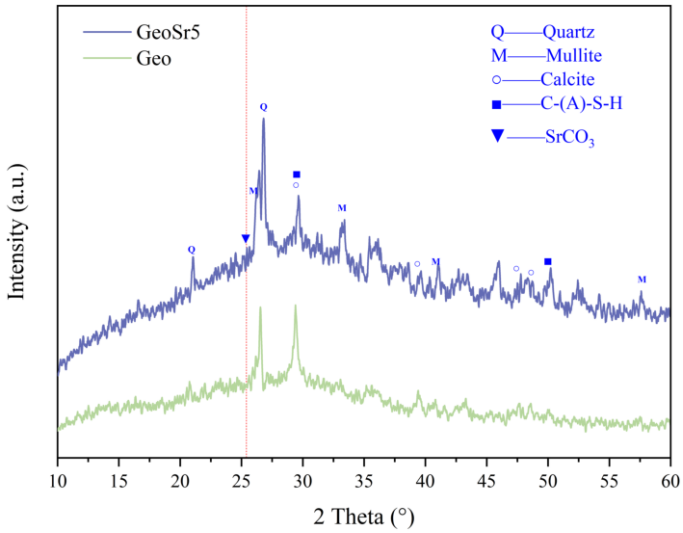

Fig.13 The XRD patterns of geopolymer samples containing Sr, and without Sr.

Based on the XPS spectra of geopolymer samples with and without incorporated Sr shown in Fig.14, it can be observed that, compared to the sample Geo, the binding energies of Si 2p and Al 2p in sample GeoSr5 slightly shifted toward higher values. Specifically, the Si 2p binding energy shifted from 102.24 eV to 102.44 eV, and the Al 2p binding energy shifted from 74.05 eV to 74.22 eV. Besides, Sr 3d peaks were detected in the Sr-containing geopolymer, confirming the presence of Sr within the geopolymer matrix. According to Ref.[61], the Sr ($3d_{5/2}$) binding energy of SrO is 132.9 eV and the Sr ($3d_{5/2}$) binding energy of $SrCO_3$ is 133.4 eV. Here the existence of SrO may imply the Sr occupied the Na^+ and/or Ca^{2+} sites to balance charges. The deconvolution results provide possible supplementary evidence for the existence of $SrCO_3$.

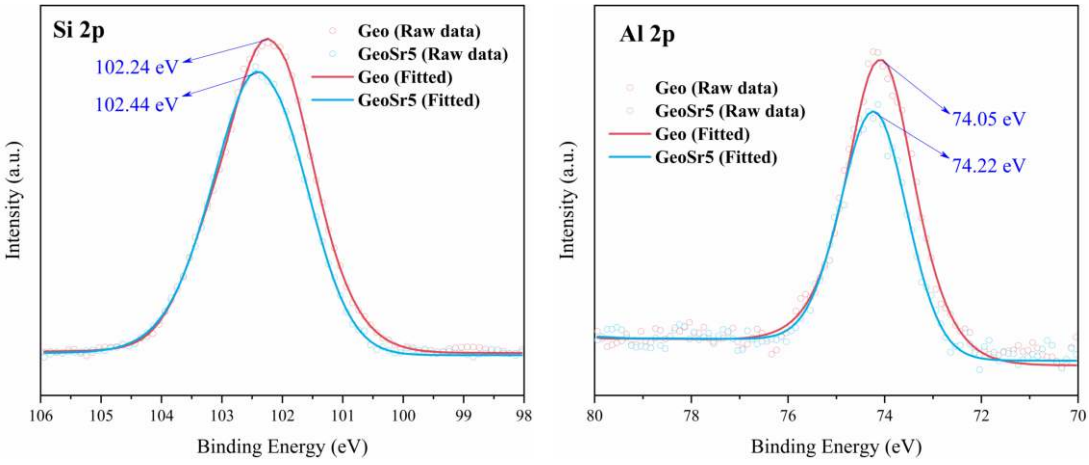

(a) Si 2p (b) Al 2p

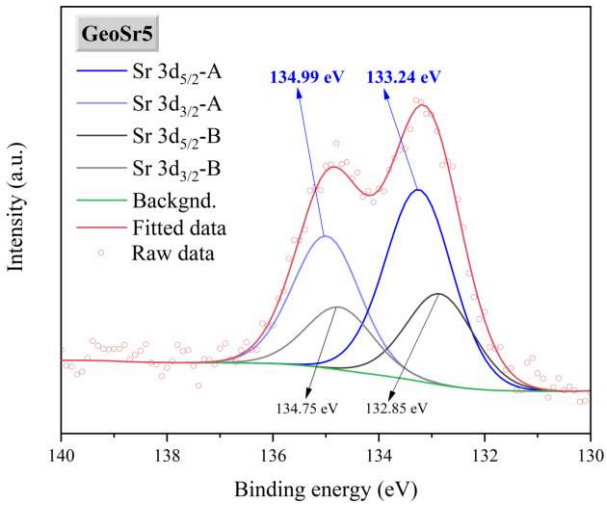

(c) Sr 3d

Fig.14 The effect of Sr incorporation on the binding energy of geopolymer

Fig.15 (a) shows the ^{29}Si MAS NMR spectrum of the Sr-containing geopolymer solidified form. The ^{29}Si NMR spectrum of GeoSr5 was deconvolved as shown in Fig.15 (b), with statistical results presented in Fig.15(c). From Fig.15(c), compared to the sample Geo the relative content of Q^0, Q^1 and Q^4(0Al) of GeoSr5 increased by 2.13%, 2.63% and 6.30%, respectively, indicating that Sr incorporation had a negative effect on the reaction process and dissolution of raw materials, thus affecting the structures of products with more short chains. Vandevenne et al. [29] also concluded that the incorporation of Sr^{2+} significantly hindered the geopolymerization kinetics. This occurred due to the rapid precipitation of $Sr(OH)_2$, as evidenced by heat release data, which consequently diminished the precursor's dissolution and thus led to a reduced polymerization reaction. Additionally, the relative content of Q^4(0Al) of GeoSr5 increased, primarily because some resonance peaks above 120 ppm were also assigned to Q^4(0Al) units during the deconvolution fitting of the ^{29}Si MAS NMR spectra. Wang et al. [46] proposed that peaks above 120 ppm arise from the strong shielding effect on the central silicon atom. This effect may result from a decreased Si-O-Si bond angle or the substitution of calcium in the coordination environment.

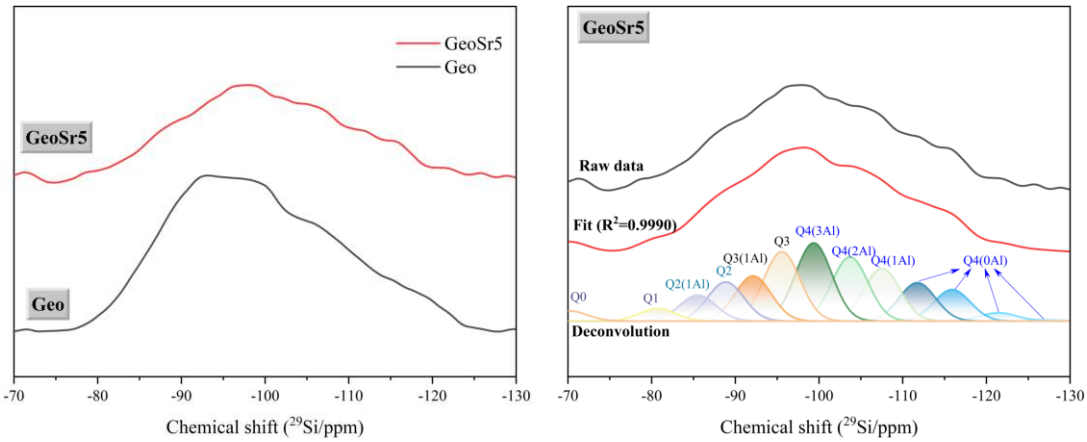

(a) ^{29}Si MAS NMR spectra of Geo and GeoSr5 (b) Deconvolved spectra of GeoSr5

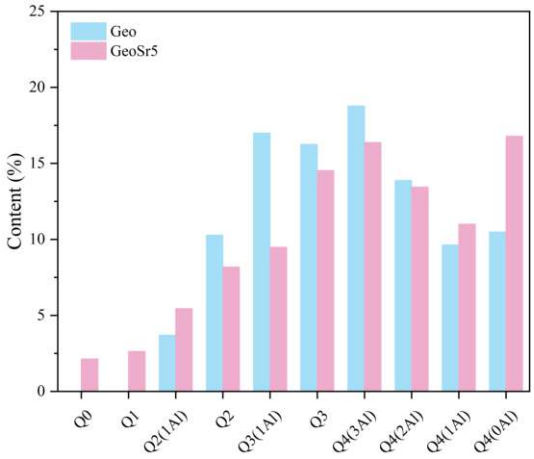

(c) Statistical results from deconvolved spectra

538 Fig.15 The effect of Sr incorporation on the ^{29}Si MAS NMR spectra of geopolymer sample

539 From Fig.15(c), upon incorporation of Sr, the relative content of Q^3(1Al), Q^4(3Al) and Q^4(2Al)
540 decreased, while the relative content of Q^2(1Al) and Q^4(1Al) exhibited a slight increase, probably
541 indicating that a fraction of the Sr^{2+} may replace Ca^{2+} and Na^+ to form (C,Sr)-N-A-S-H and (N,Sr)-
542 A-S-H gels. Walkley et al. [33] examined the ^{29}Si MAS NMR of geopolymer samples upon
543 incorporation of Sr, and a slight reduction in Q^4(3Al) sites and consequently a slight reduction in
544 the Si/Al ratio of (N,K)-A-S-H gel were observed. These authors suggested that these effects could
545 be attributed to an enhanced charge balancing capacity, owing to the replacement of monovalent
546 alkali cations with divalent alkaline earth cations. Blackford et al. [62] reported a preferential
547 incorporation of Sr into a crystalline $SrCO_3$ phase with 1% to 2% incorporated Sr in geopolymer. A

548 recent study by Geddes et al. [32] reported that the effect of Sr^{2+} on geopolymers depended on its
549 content. When Sr/Na>0.005, geopolymer immobilized Sr via dual mechanisms: bind Sr within
550 geopolymer gel chemically and encapsulate excess Sr in the form of $SrCO_3$ physically.

551 Based on the above results, in this work, with 5 wt% $SrCl_2 \cdot 6H_2O$ incorporation, from XRD
552 and XPS results, $SrCO_3$ was generated, and from the ^{29}Si MAS NMR deconvolved results, (C,Sr)-
553 N-A-S-H, (N,Sr)-A-S-H may also exist. The incorporation of Sr^{2+} significantly affected the
554 geopolymerization process, leading to the decreased relative intensity of the reflections (~29°)
555 representing C-(A)-S-H and calcite in XRD results and the presence of Q^0 and Q^1 from the
556 deconvolved ^{29}Si MAS NMR results. Therefore, the geopolymers would simultaneously immobilize
557 Sr within (C,Sr)-N-A-S-H and (N,Sr)-A-S-H gels chemically, and encapsulate excess Sr in the form
558 of $SrCO_3$ physically. This encapsulation mechanism thus provided a highly effective barrier against
559 the leaching of Sr^{2+} from the geopolymer matrix [63].

560 3.5 The leaching behavior of stable and radioactive Sr-containing
561 samples

562 3.5.1 Samples with stable Sr

563 The leaching rates and CFL over time for geopolymer and cement solidified forms with
564 incorporated stable Sr are presented in Fig.16. The leaching rate of Sr-containing geopolymer
565 solidified forms is significantly lower than that of cement, by two orders of magnitude. For
566 geopolymer solidified forms with Sr (GeoSr5), the initial leaching rate in simulated underground
567 water was lower than that in Milli Q water. However, after a leaching period exceeding 7 days, the
568 leaching rate of GeoSr5 in simulated underground water became higher, which may involve the
569 dissolution of $SrCO_3$ in the simulated underground water. Shirota et al. [64] reported that the polar

570 (110) and (010) faces of $SrCO_3$ were not stable under acidic condition by Atomic Force Microscopy

571 (AFM) observation. The results of Andrade et al. [65] also evidenced the dissolution of strontium

572 carbonate would be promoted with pH reduced. Interestingly, for cement solidified forms with Sr

573 (CemSr5), the leaching rates in simulated underground water were slightly lower than those in Milli

574 Q water.

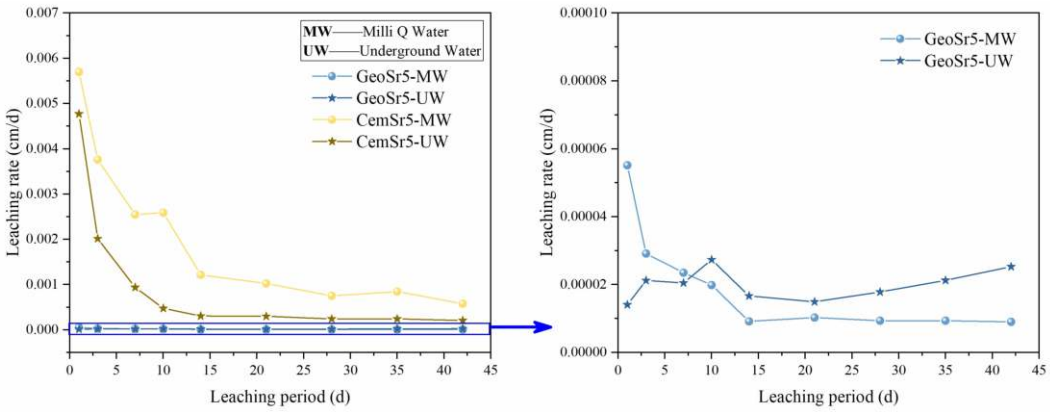

(a) Leaching rate

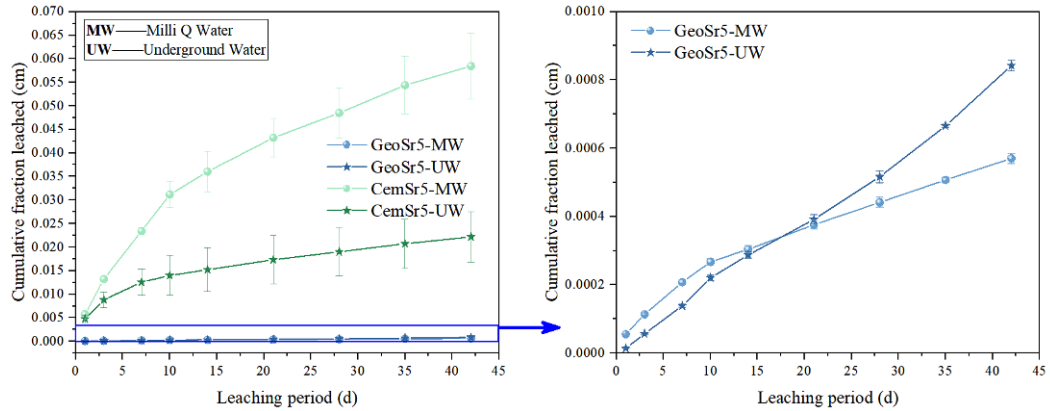

(b) Cumulative fraction leached

575 Fig.16 The leaching rate (a) and cumulative fraction leached (b) of samples containing Sr

576 The leaching data shown in Fig.16 were fitted with different mathematical models (diffusion

577 model, dissolution model and their combination model) based on Eq. (3)~(8), with results shown in

578 Fig.17 and Table 7.

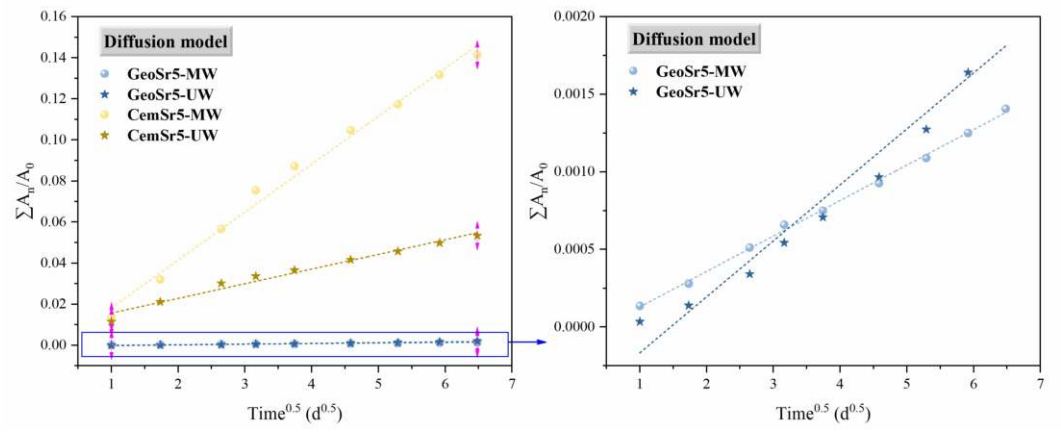

579

580 （a）DFM

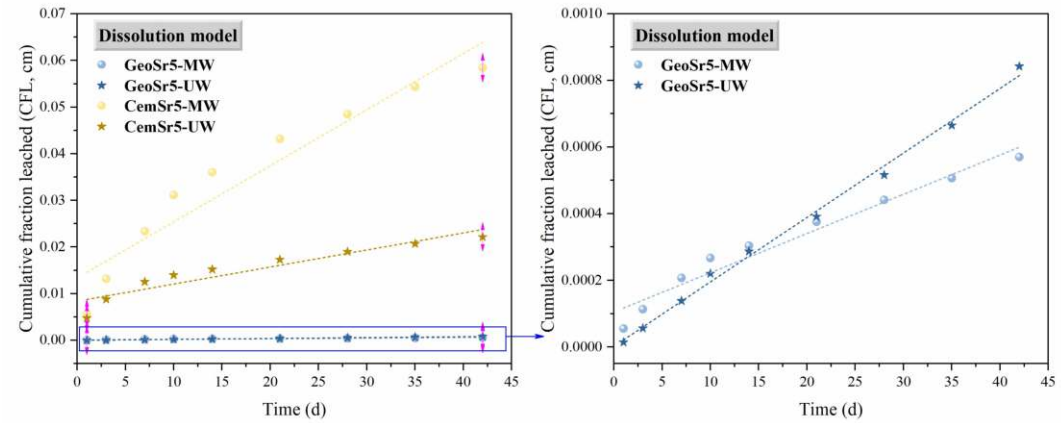

581

582 （b）DSM

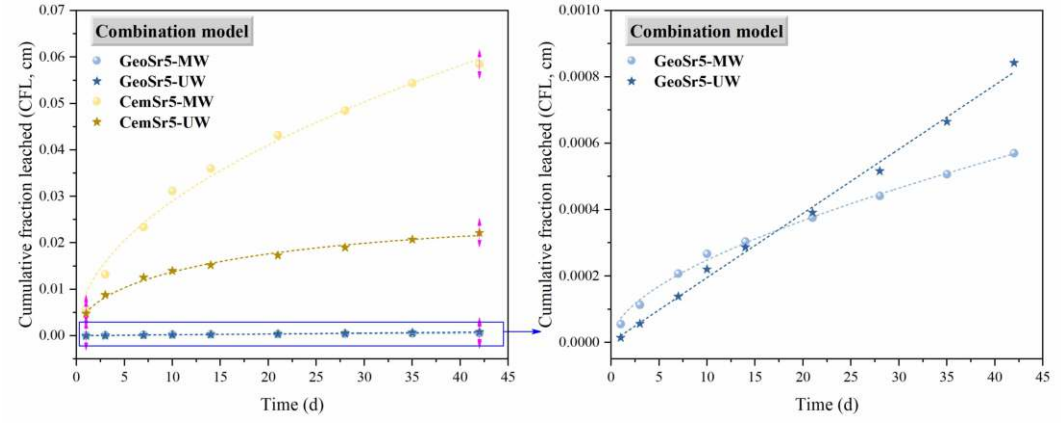

583

584 （c）DFM+DSM

585 Fig.17 Fitting results of samples containing Sr by a diffusion model, dissolution model and combination model

586

Table 7 R^2 of samples containing Sr derived from leaching models

Sample ID	DFM		DSM		DFM+DSM
	D (cm^2/s)	R^2	U (cm^2/d)	R^2	R^2
GeoSr5-MW	7.80E-14	0.9976	4.78E-06	0.9550	0.9954
GeoSr5-UW	1.95E-13	0.9477	7.85E-06	0.9948	0.9948
CemSr5-MW	8.45E-10	0.9902	4.96E-04	0.9068	0.9871
CemSr5-UW	8.00E-11	0.9714	1.52E-04	0.8661	0.9913

According to Table 7, when geopolymer solidified forms were leached in Milli Q water (GeoSr5-MW), the correlation coefficient given by fitting the diffusion model was higher, indicating that diffusion may be the primary mechanism driving the leaching of Sr^{2+} by Milli Q water. However, for geopolymer solidified forms with stable Sr leached in simulated underground water (GeoSr5-UW), the dissolution behavior cannot be overlooked since the dissolution model or the combined model was more suitable for describing leaching behavior. According to the fitting results, the diffusion coefficients of geopolymer obtained from the diffusion model in Milli Q water (MW) and simulated underground water (UW) are 7.8E-14 cm^2/s and 1.95E-13 cm^2/s, respectively, and the dissolution rates obtained from the dissolution model in MW and UW are 4.78E-06 cm^2/d and 7.85E-06 cm^2/d, respectively. From these results, it can be concluded that both the diffusion coefficient and the dissolution rate of the geopolymer containing stable Sr in simulated underground water are greater than those in Milli Q water. For cement solidified forms, the leaching behavior in Milli Q water was primarily controlled by the diffusion mechanism, while the combined model was more appropriate for describing the leaching behavior in simulated underground water.

3.5.2 Samples with radioactive ^{90}Sr

The leaching rates and CFL of ^{90}Sr are presented in Table 8. Strontium-90 was only detected in leachate when the leaching period was 1 day (for the simulated underground water leachant), as shown in Table 8, indicating that the compared to cement, geopolymer demonstrated a superior

606 capacity for immobilizing ^{90}Sr.

607 Table 8 The leaching rate and cumulative fraction leached of geopolymer and cement samples containing ^{90}Sr

Leaching period (d)	Leaching rate (cm/d)				Cumulative fraction leached (cm)			
	CemSr90-MW	CemSr90-UW	GeoSr90-MW	GeoSr90-UW	CemSr90-MW	CemSr90-UW	GeoSr90-MW	GeoSr90-UW
0.125	2.26E-03	2.75E-03	-	-	2.83E-04	3.44E-04	-	-
1	8.73E-04	8.91E-04	-	9.14E-05	1.05E-03	1.12E-03	-	9.14E-05
2	4.58E-04	3.36E-04	-	-	1.50E-03	1.46E-03	-	-
3	3.13E-04	1.99E-04	-	-	1.82E-03	1.66E-03	-	-
6	1.35E-04	9.93E-05	-	-	2.22E-03	1.96E-03	-	-

608 Note："-" represents "not detected".

609 3.6 The effect of leaching on the structural evolution of Sr-
610 containing geopolymer

611 Fig.18 presents high-resolution XPS spectra of Si 2p, Al 2p and Sr 3d in Sr-containing
612 geopolymer solidified forms after the leaching tests. For the geopolymer samples leached in Milli
613 Q water, the binding energy peaks of Al 2p and Si 2p changed only slightly, meaning minimal
614 structural alterations in the geopolymer samples after leaching in Milli Q water. In contrast, for the
615 geopolymer samples leached in simulated underground water, the binding energy peaks of Al 2p
616 and Si 2p shifted toward higher values, suggesting more significant structural changes in the
617 geopolymer sample when exposed to simulated underground water. The binding energy peak of Sr
618 3d shifted toward higher values after the leaching tests. The peak deconvolutions of the Sr 3d high-
619 resolution spectra of the leached samples were also performed. According to Ref. [61], the Sr ($3d_{5/2}$)
620 binding energy of SrO is 132.9 eV, while that of $SrCO_3$ is 133.4 eV. In the deconvolution results,
621 the Sr 3d-A peak corresponded to $SrCO_3$, whereas the Sr 3d-B peak corresponded to SrO. Compared
622 with sample GeoSr5, the sample leached in simulated underground water (GeoSr5-UW) exhibited
623 a decrease in the relative area of the Sr 3d-A peak (blue lines), which provides supplementary

evidence for the possible dissolution of $SrCO_3$ in simulated underground water. Quantitatively, the relative contents of Sr 3d-A and Sr 3d-B were calculated. For GeoSr5, the relative contents of Sr 3d-A and Sr 3d-B were 32.18% and 67.82%, respectively. And for GeoSr5-UW, the relative contents of Sr 3d-A and Sr 3d-B were 68.17% and 31.83%, respectively. This may indicate that the relative contents of $SrCO_3$ decreased by 35.99% when leached in simulated underground water.

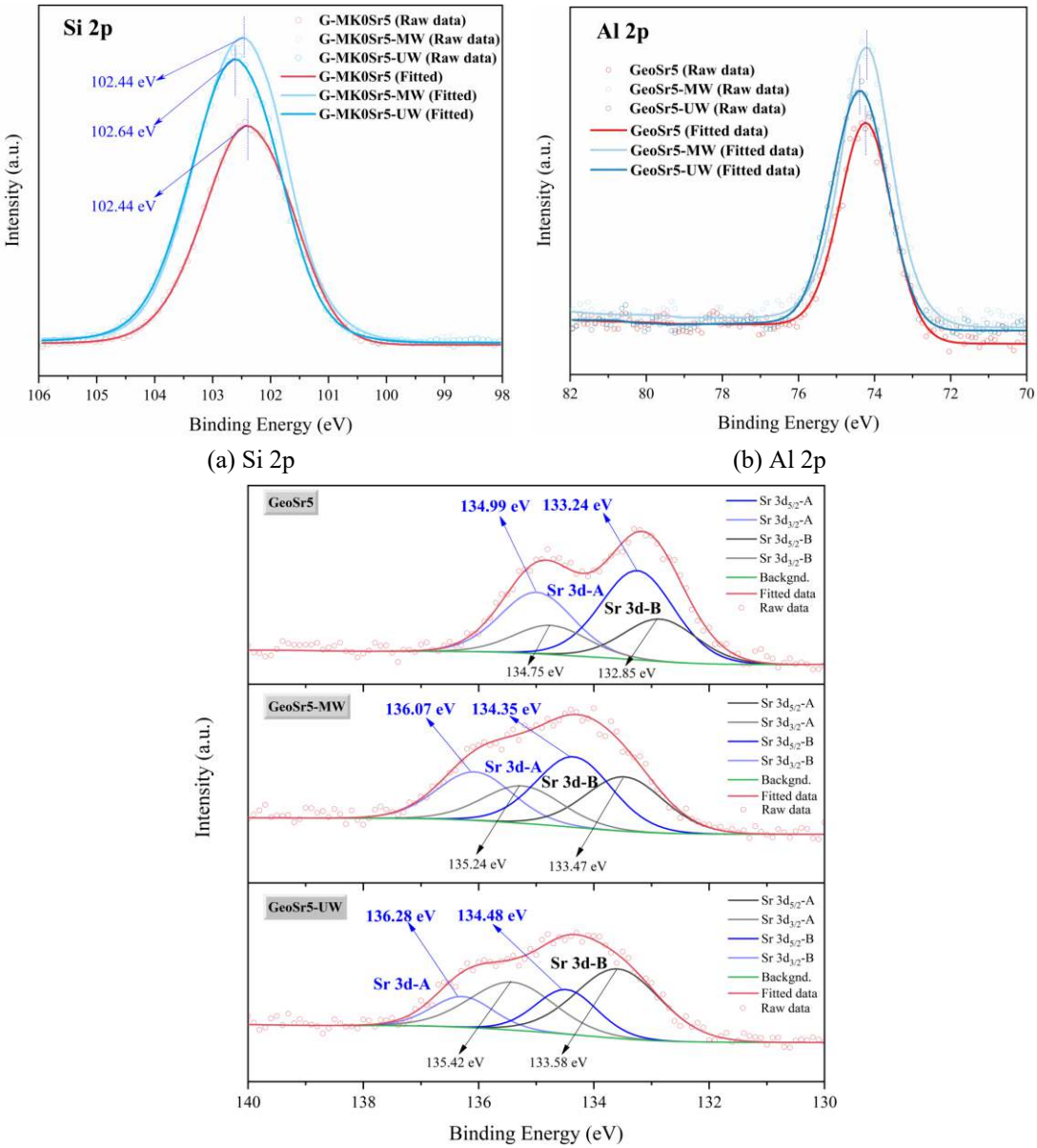

(a) Si 2p (b) Al 2p

(c) Sr 3d

Fig.18 The XPS spectra of geopolymer samples containing Sr after leaching experiments

To further clarify the molecular structural changes of geopolymer samples with stable Sr after

631 the leaching tests, MAS NMR analysis was conducted on the leached samples. The ^{29}Si MAS NMR

632 spectra of the Sr-containing geopolymers before and after leaching are shown in Fig.19, and the

633 relative contents of different [SiO_4] chemical environments after deconvolution are presented in

634 Fig.19.

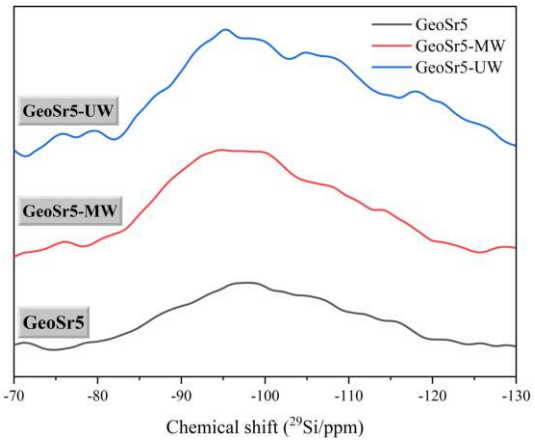

(a) ^{29}Si MAS NMR spectra of Sr-containing geopolymer before and after leaching

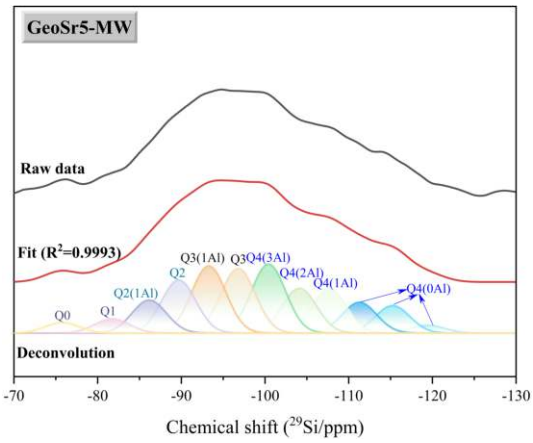

(b) deconvolved spectra of Sr-containing geopolymer after leaching in MW

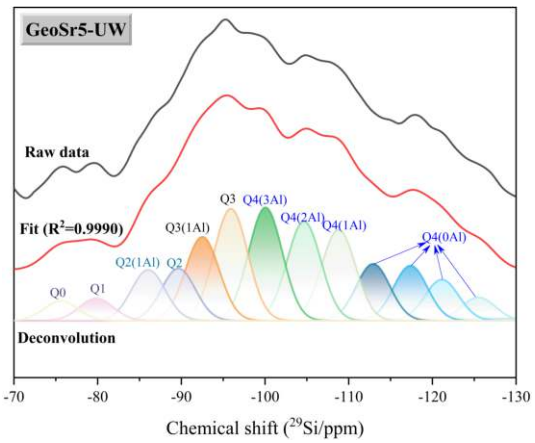

(c) deconvolved spectra of Sr-containing geopolymer after leaching in UW

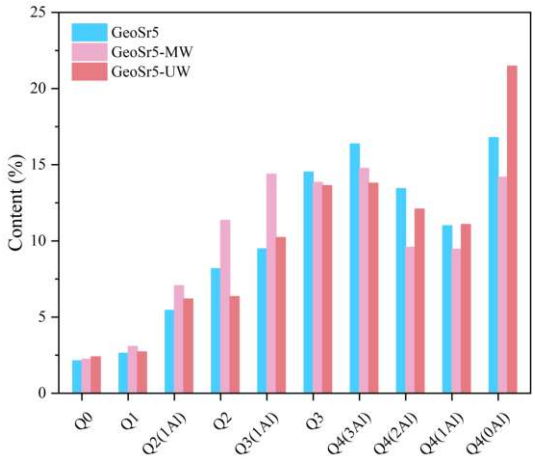

(d) the statistical results from above deconvolved spectra

635 Fig.19 ^{29}Si MAS NMR spectra of geopolymer samples containing Sr after leaching experiments

636 Fig. 19(a) illustrates the ^{29}Si MAS NMR spectra of Sr-containing geopolymers before leaching

637 and after leaching in MW (Milli Q water) and UW (simulated underground water), with their

corresponding deconvolved spectra presented in Fig. 19(b) and Fig. 19(c). The relative contents of structural units derived from deconvolved spectra are summarized in Fig. 19(d). Similar to the Cs-containing samples after leaching, Sr-containing samples exhibit sharper spectral profiles after leaching in simulated underground water, compared to samples leached in Milli Q water (Fig. 19(a)). After the leaching test, the ^{29}Si MAS NMR spectra of the geopolymer samples (Fig. 19(d)) both exhibited a slight increase of Q^0, suggesting that partial structural disintegration may have occurred during the leaching process, which is consistent with the previous fitting results. Sr-containing geopolymer samples showed differential structural evolution mechanisms under different leaching media. For the sample leached in Milli Q water (GeoSr5-MW), the relative contents of Q^2 and Q^3(1Al) units increase, and both crosslinked main chain length (MCL_C) and non-crosslinked main chain lengths (MCL_{NC}) extend after leaching according to calculated results in Table 4, with a decreased Si/Al ratio of C-(N)-A-S-H gel, suggesting structural reorganization and repolymerization to form a gel with increased Al content [46]. In contrast, samples leached in simulated underground water exhibit slightly decreased cross-linked and non-cross-linked main chain lengths from Table 4, indicating structural dissolution and possible $SrCO_3$ leaching in underground water, which is also consistent with the higher dissolution rate leaching in simulated underground water fitted by the leaching models.

3.7 Retention mechanisms of Cs and Sr in geopolymer

Table 9 displays the CFL of samples containing stable and radioactive Cs and Sr.

Table 9 Cumulative fraction leached (CFL) of samples with stable and radioactive Cs and Sr

Samples	CFL in Milli Q water (cm)			CFL in simulated underground water (cm)		
	1d	7d	42d	1d	7d	42d
GeoCs5	0.02449	0.04502	0.06639	0.02292	0.04560	0.07163
CemCs5	0.06121	0.17094	0.27137	0.08688	0.19441	0.26675

GeoCs137	0.00134	0.00370	/	0.00009	0.00295	/
CemCs137	0.00918	0.01830	/	0.00781	0.02410	/
GeoSr5	0.00006	0.00021	0.00057	0.00001	0.00014	0.00084
CemSr5	0.00570	0.02341	0.05844	0.00477	0.01256	0.02217
GeoSr90	-	- (6d)	/	0.00009	- (6d)	/
CemSr90	0.00105	0.00222 (6d)	/	0.00112	0.00196 (6d)	/

Note：“-” represents “not detected”; “/” represents “no experiments”.

Based on CFL results of cement and geopolymer leached in Milli Q water (MW) and simulated underground water (UW), two key conclusions can be summarized: (1) Cs is more mobile than Sr no matter whether it is immobilized in cement or geopolymer since the CFL of Cs exceeded that of Sr by about 2 orders of magnitude over the same leaching periods; (2) geopolymer exhibited improved immobilization of stable and radioactive Cs and Sr compared to cement, especially for Sr immobilization.

According to MAS NMR deconvolution results, the geopolymer system comprises coexisting C-(N)-A-S-H and N-A-S-H gels. Fig.20 displays a schematic two-dimensional presentation of retention mechanisms for Cs and Sr in C-(N)-A-S-H gel and N-A-S-H gel, and this discussion focuses specifically on how Cs^{+} and Sr^{2+} is bound into and leached out from these two kinds of gels from the perspective of their structural evolution. Notably, while other ions (e.g., Na^{+}, Al^{3+}, Ca^{2+}) would also leach concurrently during the leaching process, only potential alterations related to Cs^{+} and Sr^{2+} are highlighted here. From the results of Section 3.1 and Section 3.4, Cs incorporation altered the local environment of Al, and the larger Cs ionic radius may suggest a tendency for the likely formation of (N,Cs)-A-S-H. The incorporation of Sr^{2+} affected the geopolymerization process, consuming OH^{-} and then generating $SrCO_3$. Geopolymers may simultaneously chemically bind Sr within (C,Sr)-N-A-S-H and (N,Sr)-A-S-H gels, as well as physically encapsulate $SrCO_3$. In summary, Cs and Sr are apparently immobilized in geopolymers through chemical binding and

physical encapsulation mechanisms, with a portion of ions remaining retained within the pores.

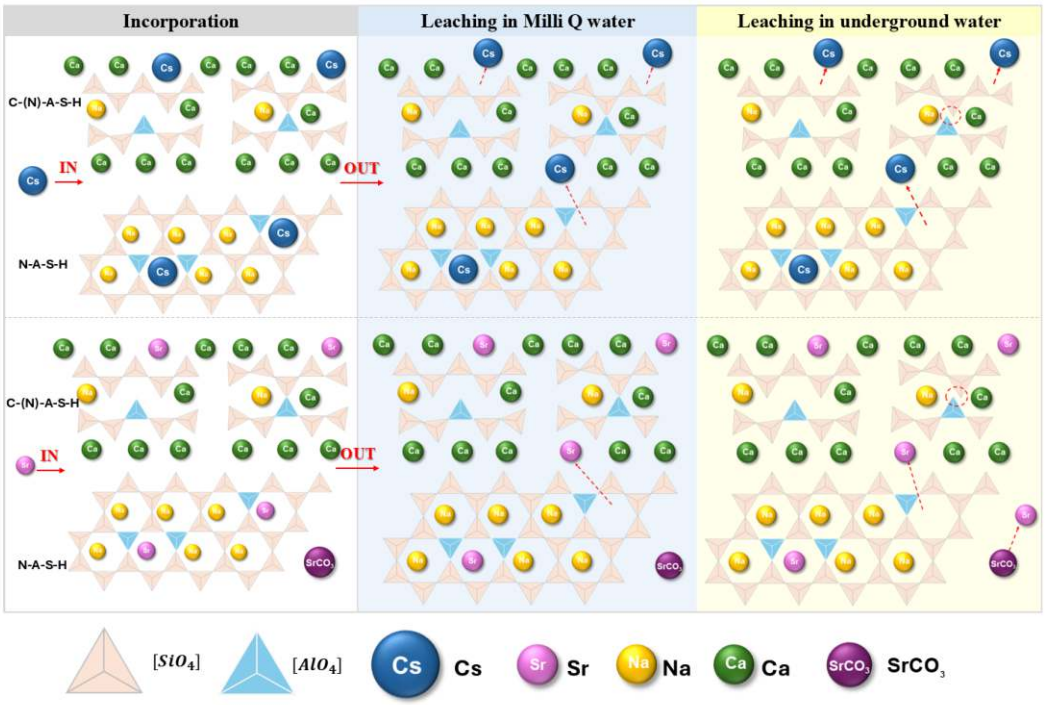

Fig.20 Schematic two-dimensional presentation of retention mechanisms of Cs and Sr in C-(N)-A-S-H gel and N-A-S-H gel.

During the leaching process, nuclides retained in the pores would be released from the geopolymer-solidified wasteform via diffusion. When leached in simulated underground water (UW), the diffusion rate driven by concentration gradients decreases due to the presence of abundant competing ions in the UW. Consequently, at the early stages, geopolymers generally exhibit slightly lower leaching rates for Cs, ^{137}Cs, and Sr in UW compared to those in Milli Q water (MW). However, when using geopolymer for ^{90}Sr immobilization experiments, detectable activity was observed only during the first day of leaching in UW over the entire 6-day period, suggesting that the immobilization mechanisms for stable and radioactive nuclides may not always align completely, warranting further investigation. In addition to diffusion, leaching model fitting results indicate that dissolution behavior cannot be neglected, probably involving phase transformation/reorganization of the gel matrix and $SrCO_3$ dissolution in the UW. This dissolution behavior is evidenced by the

692 emergence of Q^0 species in deconvolved ^{29}Si MAS NMR spectra from leached geopolymer samples.

693 The XPS results of Cs-containing geopolymer samples demonstrate that after leaching, the
694 binding energies consistently shifted toward higher values, with minimal influence from the
695 leaching medium (MW vs. UW). This observation suggests that Cs-containing geopolymers
696 undergo gel structural transformations during leaching in both MW and UW. Notably, MAS NMR
697 analysis revealed more pronounced gel structural alterations in UW compared to MW. For Sr-doped
698 systems, XPS spectra showed negligible shifts in Si and Al binding energies after MW leaching,
699 whereas UW leaching induced upward shifts in these binding energies. Combined with MAS NMR
700 deconvolution data, the limited structural impact of MW leaching may arise from localized
701 structural reorganization. When leached in UW, for both Cs- and Sr-containing samples, a slight
702 reduction in cross-linking chain lengths occurs (Table 4), implying potential transformation of the
703 C-(N)-A-S-H gel induced by UW. However, distinct Si/Al ratio trends emerged between the Cs- and
704 Sr-containing samples. For the Cs-containing sample (GeoCs5), the Si/Al ratio of C-(N)-A-S-H gel
705 increased alongside reduced chain lengths after leaching in UW, indicating Cs^+ may facilitate Al
706 leaching from the gel structure. While for GeoSr5, after leaching in UW, both the Si/Al ratio of the
707 C-(N)-A-S-H gel and MCL_C slightly decreased, suggesting the newly reunited gel involved higher
708 Al contents.

709 4. Conclusions and prospects

710 In this study, 5 wt% $CsNO_3$ and $SrCl_2 \cdot 6H_2O$ were incorporated into geopolymer with
711 subsequent examination of the geopolymerisation products and gel structures, after which leaching
712 experiments in Milli Q water (MW) and simulated underground water (UW) were carried out to
713 understand the retention mechanism of Cs and Sr in geopolymer from the perspective of products

714 evolution. Radioactive ^{137}Cs and ^{90}Sr were also incorporated and leaching experiments carried out
715 to examine ^{137}Cs and ^{90}Sr immobilization by the geopolymer material. The following key
716 conclusions can be drawn from the results:

717 (1) Upon incorporation of Cs, no significant changes in the main geopolymer material phases
718 can be detected from XRD results. From XPS and MAS NMR results, Cs incorporation altered the
719 local environment of Al, and the larger Cs ionic radius may generate a tendency for the formation
720 of (N,Cs)-A-S-H when Cs is incorporated. Unlike Cs, the incorporation of Sr^{2+} clearly affected the
721 geopolymerization process, the geopolymers would simultaneously immobilize Sr within (C,Sr)-N-
722 A-S-H and (N,Sr)-A-S-H gels chemically, and encapsulate excess Sr in the form of $SrCO_3$ physically.
723 Therefore, Cs and Sr are immobilized in geopolymers through chemical binding and physical
724 encapsulation mechanisms, with a portion of ions remaining retained within the pores.

725 (2) According to the fitting results of leaching models and products evolution results from XPS
726 and MAS NMR experiments, diffusion and dissolution mechanisms governed Cs^+ leaching from
727 the geopolymer. Cs-containing geopolymers undergo gel structural transformations during leaching
728 in both MW and UW, while Cs^+ may facilitate Al release in UW with an increased Si/Al ratio of C-
729 (N)-A-S-H gel and reduced the main chain lengths. Diffusion is likely the primary mechanism
730 driving the leaching of Sr^{2+} from geopolymer in Milli Q water, involving localized structural
731 reorganization with increased main chain length. Dissolution behavior cannot be ignored during
732 leaching in UW, probably involving gels transformation/reorganization and $SrCO_3$ dissolution.

733 (3) For stable- and radioactive- Cs and Sr, Cs is more mobile than Sr since the cumulative
734 fraction leached of Cs exceeded that of Sr by about 2 orders of magnitude over the same leaching
735 periods. Geopolymer exhibited better immobilization of stable- and radioactive- Cs and Sr than

cement, especially for Sr immobilization. However, slightly divergent results were observed when comparing the stable isotope with radionuclide data, indicating that the immobilization mechanisms for stable and radioactive nuclides may not always align completely, warranting further investigation by incorporating radioactive isotopes rather than radioactive simulants.

Overall, this study provides a product evolution perspective on Cs and Sr incorporation into geopolymer materials and their subsequent leaching behavior, offering an improved structural understanding of the retention mechanism of Cs and Sr in geopolymers. However, leaching tests with radioactive nuclides were only conducted for 7 days, and leaching tests with stable nuclides for 42 days in this work. While this is sufficient to examine early-stage leaching and structural changes, longer-term tests are required to evaluate long-term material stability for real disposal or storage applications. In future studies, Ca, Si and Al concentrations in leachates should also be measured and considered to understand the leaching behaviors of these elements with the incorporation of nuclides, providing a fuller view of aluminosilicate structure degradation. Finally, stable analogues are widely used, rather than radioactive isotopes, in the testing of cementitious and other immobilization matrices (due largely to health and safety considerations). However, the slightly divergent results between stable isotope and radionuclide data were observed in this work, therefore, our work indicates that using stable analogues may not quantitatively simulate the incorporation and immobilization of radioactive species at lower mass concentrations.

CRediT authorship contribution statement

Guiyan Xiong: Conceptualization, Formal analysis, Methodology, Investigation, Visualization, Writing-Original Draft, Writing-Reviewing and Editing.

Andrew B. Cundy: Conceptualization, Methodology, Validation, Writing-Original Draft, Writing-Reviewing and Editing, Supervision, Funding acquisition.

Xiaolu Guo: Conceptualization, Methodology, Supervision, Validation, Writing-Original Draft, Writing-Reviewing and Editing, Funding acquisition.

Acknowledgement

The authors acknowledge the financial support received from the National Natural Science Foundation of China (No. 52578318, 12411530113 and 52178241), a project supported by Scientific Research Fund of Hunan Provincial Education Department (No. 25C0110), also EU SURRI project (project 101079345) and NNUF-EXACT (EPSRC EP/T011548/1). Thanks are extended to the GAU-Radioanalytical Laboratories and staff.

References

[1] Plans For New Reactors Worldwide - World Nuclear Association, (n.d.). https://world-nuclear.org/information-library/current-and-future-generation/plans-for-new-reactors-worldwide (accessed July 25, 2025).

[2] National Nuclear Safety Admission. National Nuclear Power Operation Status (January-June 2025), (n.d.). https://nnsa.mee.gov.cn/ywdt/hyzx/202508/t20250808_1125164.html (accessed November 18, 2025).

[3] S. Li, Y. Ni, Q. Guo, Plutonium in the coastal seawater around Chinese nuclear power plants: Sources, distribution, and environmental implications, Marine Pollution Bulletin 207 (2024) 116882. https://doi.org/10.1016/j.marpolbul.2024.116882.

[4] J. Kirk, R. Clayton, A. Banford, L. Stamford, Environmental impacts of decommissioning a nuclear power plant: A life cycle assessment of a Magnox site, Environmental Impact Assessment Review 113 (2025) 107880. https://doi.org/10.1016/j.eiar.2025.107880.

[5] D. Dong, Z. Wang, J. Guan, Y. Xiao, Research on safe disposal technology and progress of radioactive nuclear waste, Nuclear Engineering and Design 435 (2025) 113934. https://doi.org/10.1016/j.nucengdes.2025.113934.

[6] J. Li, L. Chen, J. Wang, Solidification of radioactive wastes by cement-based materials, Progress in Nuclear Energy 141 (2021) 103957. https://doi.org/10.1016/j.pnucene.2021.103957.

[7] S. Le Caër, L. Dezerald, K. Boukari, M. Lainé, S. Taupin, R.M. Kavanagh, C.S.N. Johnston, E. Foy, T. Charpentier, K.J. Krakowiak, R.J.-M. Pellenq, F.J. Ulm, G.A. Tribello, J. Kohanoff, A. Saúl, Production of H2 by water radiolysis in cement paste under electron irradiation: A joint experimental and theoretical study, Cement and Concrete Research 100 (2017) 110–118. https://doi.org/10.1016/j.cemconres.2017.05.022.

[8] B. Kim, B. Lee, C.-M. Chon, S. Lee, Compressive Strength Properties of Geopolymers from Pond Ash and Possibility of Utilization as Synthetic Basalt, J. Korean Ceram. Soc 56 (2019) 365–373. https://doi.org/10.4191/kcers.2019.56.4.03.

[9] B. Kim, B. Walkley, J.L. Provis, H. Ma, W. Um, Effect of Ca(OH)2 on the immobilization of simulated radioactive borate waste in metakaolin-based geopolymer waste forms, Cement and Concrete Research 197 (2025) 107946. https://doi.org/10.1016/j.cemconres.2025.107946.

[10] S. Ukritnukun, C.C. Sorrell, D. Gregg, E.R. Vance, P. Koshy, Potential Use of Ambient-Cured Geopolymers for Intermediate Level Nuclear Waste Storage, MRS Advances 3 (2018) 1123–1131. https://doi.org/10.1557/adv.2018.276.

[11] D. Perera, E. Vance, S. Kiyama, Z. Aly, P. Yee, Geopolymers as Candidates for the Immobilisation of Low- and Intermediate-Level Waste, MRS Online Proceedings Library 985 (2007) 1001. https://doi.org/10.1557/PROC-985-0985-NN10-01.

[12] X. Niu, Y. Elakneswaran, A. Li, S. Seralathan, R. Kikuchi, Y. Hiraki, J. Sato, T. Osugi, B. Walkley, Incorporation of boron into metakaolin-based geopolymers for radionuclide immobilisation and neutron capture potential, Cement and Concrete Research 190 (2025) 107814. https://doi.org/10.1016/j.cemconres.2025.107814.

[13] N. Kozai, J. Sato, T. Osugi, I. Shimoyama, Y. Sekine, F. Sakamoto, T. Ohnuki, Sewage sludge ash contaminated with radiocesium: Solidification with alkaline-reacted metakaolinite (geopolymer) and Portland cement, Journal of Hazardous Materials 416 (2021) 125965.

https://doi.org/10.1016/j.jhazmat.2021.125965.
[14] S. Zhou, J. Li, L. Rong, J. Xiao, Y. Liu, Y. Duan, L. Chu, Q. Li, L. Yang, Immobilization of uranium soils with alkali-activated coal gangue–based geopolymer, J Radioanal Nucl Chem 329 (2021) 1155–1166. https://doi.org/10.1007/s10967-021-07812-x.
[15] A. Santi, E. Mossini, G. Magugliani, F. Galluccio, E. Macerata, P. Lotti, G.D. Gatta, D. Vadivel, D. Dondi, D. Cori, H. Nonnet, M. Mariani, Design of sustainable geopolymeric matrices for encapsulation of treated radioactive solid organic waste, Frontiers in Materials 9 (2022). https://www.frontiersin.org/articles/10.3389/fmats.2022.1005864 (accessed March 9, 2023).
[16] H. Hamdane, M. Oumam, H.S. Mhamdi, A. Bouih, T. El Ghailassi, R. Boulif, J. Alami, B. Manoun, H. Hannache, Elaboration of geopolymer package derived from uncalcined phosphate sludge and its solidification performance on nuclear grade resins loaded with 134Cs, Science of The Total Environment 857 (2023) 159313. https://doi.org/10.1016/j.scitotenv.2022.159313.
[17] M. De Campos, C. Reeb, C.A. Davy, J. Hosdez, D. Lambertin, Solidification/stabilization (S/S) of high viscosity organics in geopolymers, Journal of Nuclear Materials 571 (2022) 153979. https://doi.org/10.1016/j.jnucmat.2022.153979.
[18] W. Lin, H. Chen, C. Huang, Performance study of ion exchange resins solidification using metakaolin-based geopolymer binder, Progress in Nuclear Energy 129 (2020) 103508. https://doi.org/10.1016/j.pnucene.2020.103508.
[19] W.-H. Lee, T.-W. Cheng, Y.-C. Ding, K.-L. Lin, S.-W. Tsao, C.-P. Huang, Geopolymer technology for the solidification of simulated ion exchange resins with radionuclides, Journal of Environmental Management 235 (2019) 19–27. https://doi.org/10.1016/j.jenvman.2019.01.027.
[20] V. Cuccia, C.B. Freire, A.C.Q. Ladeira, Radwaste oil immobilization in geopolymer after non-destructive treatment, Progress in Nuclear Energy 122 (2020) 103246. https://doi.org/10.1016/j.pnucene.2020.103246.
[21] V. Cantarel, F. Nouaille, A. Rooses, D. Lambertin, A. Poulesquen, F. Frizon, Solidification/stabilisation of liquid oil waste in metakaolin-based geopolymer, Journal of Nuclear Materials 464 (2015) 16–19. https://doi.org/10.1016/j.jnucmat.2015.04.036.
[22] J.L. Provis, 19 - Immobilisation of toxic wastes in geopolymers, in: J.L. Provis, J.S.J. van Deventer (Eds.), Geopolymers, Woodhead Publishing, 2009: pp. 421–440. https://doi.org/10.1533/9781845696382.3.421.
[23] E. Mukiza, Q.T. Phung, S.C. Seetharam, T.N. Nguyen, C. Bruggeman, G. De Schutter, Recent advances in immobilization of radioactive cesium and strontium-bearing wastes in alkali activated materials – A review, Journal of Environmental Management 370 (2024) 122746. https://doi.org/10.1016/j.jenvman.2024.122746.
[24] S. Liu, J. Zu, G. Han, X. Pan, Y. Xue, J. Diao, Q. Tang, M. Jin, Ammonium phosphomolybdate-modified UiO-66 as an efficient adsorbent for the selective removal of 137Cs from radioactive wastewater, Separation and Purification Technology 329 (2024) 125073. https://doi.org/10.1016/j.seppur.2023.125073.
[25] S.D. Hemming, J.M. Purkis, P.E. Warwick, A.B. Cundy, Current and emerging technologies for the remediation of difficult-to-measure radionuclides at nuclear sites, Environ. Sci.: Processes Impacts 25 (2023) 1909–1925. https://doi.org/10.1039/D3EM00190C.
[26] Y. Zhu, Z. Zheng, Y. Deng, C. Shi, Z. Zhang, Advances in immobilization of radionuclide

wastes by alkali activated cement and related materials, Cement and Concrete Composites 126 (2022) 104377. https://doi.org/10.1016/j.cemconcomp.2021.104377.
[27] A. Fernandez-Jimenez, D.E. Macphee, E.E. Lachowski, A. Palomo, Immobilization of cesium in alkaline activated fly ash matrix, Journal of Nuclear Materials 346 (2005) 185–193. https://doi.org/10.1016/j.jnucmat.2005.06.006.
[28] E. Mukiza, Q.T. Phung, L. Frederickx, D. Jacques, S. Seetharam, G. De Schutter, Co-immobilization of cesium and strontium containing waste by metakaolin-based geopolymer: Microstructure, mineralogy and mechanical properties, Journal of Nuclear Materials 585 (2023) 154639. https://doi.org/10.1016/j.jnucmat.2023.154639.
[29] N. Vandevenne, R.I. Iacobescu, Y. Pontikes, R. Carleer, E. Thijssen, K. Gijbels, S. Schreurs, W. Schroeyers, Incorporating Cs and Sr into blast furnace slag inorganic polymers and their effect on matrix properties, Journal of Nuclear Materials 503 (2018) 1–12. https://doi.org/10.1016/j.jnucmat.2018.02.023.
[30] J.L. Provis, P.A. Walls, J.S.J. Van Deventer, Geopolymerisation kinetics. 3. Effects of Cs and Sr salts, Chemical Engineering Science 63 (2008) 4480–4489. https://doi.org/10.1016/j.ces.2008.06.008.
[31] M. Arbel-Haddad, Y. Harnik, Y. Schlosser, A. Goldbourt, Cesium immobilization in metakaolin-based geopolymers elucidated by 133Cs solid state NMR spectroscopy, Journal of Nuclear Materials 562 (2022) 153570. https://doi.org/10.1016/j.jnucmat.2022.153570.
[32] D.A. Geddes, M.C. Stennett, T.J. Wilkinson, B.E. Griffith, J.V. Hanna, J.L. Provis, B. Walkley, Alkali-mediated Sr incorporation mechanism and binding capacity of alkali aluminosilicate hydrate in geopolymers, Journal of Hazardous Materials 488 (2025) 137426. https://doi.org/10.1016/j.jhazmat.2025.137426.
[33] B. Walkley, X. Ke, O.H. Hussein, S.A. Bernal, J.L. Provis, Incorporation of strontium and calcium in geopolymer gels, Journal of Hazardous Materials 382 (2020) 121015. https://doi.org/10.1016/j.jhazmat.2019.121015.
[34] N. Deng, H. An, H. Cui, Y. Pan, B. Wang, L. Mao, J. Zhai, Effects of gamma-ray irradiation on leaching of simulated 133Cs+ radionuclides from geopolymer wasteforms, Journal of Nuclear Materials 459 (2015) 270–275. https://doi.org/10.1016/j.jnucmat.2015.01.052.
[35] Q. Li, Z. Sun, D. Tao, Y. Xu, P. Li, H. Cui, J. Zhai, Immobilization of simulated radionuclide 133Cs+ by fly ash-based geopolymer, Journal of Hazardous Materials 262 (2013) 325–331. https://doi.org/10.1016/j.jhazmat.2013.08.049.
[36] S. Jain, N. Banthia, T. Troczynski, Conditioning of simulated cesium radionuclides in NaOH-activated fly ash-based geopolymers, Journal of Cleaner Production 380 (2022) 134984. https://doi.org/10.1016/j.jclepro.2022.134984.
[37] P. He, J. Cui, M. Wang, S. Fu, H. Yang, C. Sun, X. Duan, Z. Yang, D. Jia, Y. Zhou, Interplay between storage temperature, medium and leaching kinetics of hazardous wastes in Metakaolin-based geopolymer, Journal of Hazardous Materials 384 (2020) 121377. https://doi.org/10.1016/j.jhazmat.2019.121377.
[38] X. Liu, Y. Ding, X.L. and, Immobilization of Simulated Radionuclide 90Sr by Fly Ash-Slag-Metakaolin–Based Geopolymer, Nuclear Technology 198 (2017) 64–69. https://doi.org/10.1080/00295450.2017.1292810.
[39] Q. Tan, N. Li, Z. Xu, X. Chen, X. Peng, Q. Shuai, Z. Yao, Comparative performance of cement and metakaolin based-geopolymer blocks for strontium immobilization, Journal of the Ceramic

Society of Japan 127 (2019) 44–49. https://doi.org/10.2109/jcersj2.18130.
[40] S. Jain, N. Banthia, T. Troczynski, Leaching of immobilized cesium from NaOH-activated fly ash-based geopolymers, Cement and Concrete Composites 133 (2022) 104679. https://doi.org/10.1016/j.cemconcomp.2022.104679.
[41] M. Komljenović, G. Tanasijević, N. Džunuzović, J.L. Provis, Immobilization of cesium with alkali-activated blast furnace slag, Journal of Hazardous Materials 388 (2020) 121765. https://doi.org/10.1016/j.jhazmat.2019.121765.
[42] JTG 3441-2024 Test Methods of Materials Stabilized with Inorganic Binders, (n.d.). http://www.csres.com/detail/407803.html (accessed November 18, 2025).
[43] J.D. Chaplin, D. Berillo, J.M. Purkis, M.L. Byrne, A.D.C.C.M. Tribolet, P.E. Warwick, A.B. Cundy, Effective 137Cs+ and 90Sr2+ immobilisation from groundwater by inorganic polymer resin Clevasol® embedded within a macroporous cryogel host matrix, Materials Today Sustainability 19 (2022) 100190. https://doi.org/10.1016/j.mtsust.2022.100190.
[44] R.O. Abdel Rahman, A.A. Zaki, Assessment of the leaching characteristics of incineration ashes in cement matrix, Chemical Engineering Journal 155 (2009) 698–708. https://doi.org/10.1016/j.cej.2009.09.002.
[45] B. Kim, J. Kang, Y. Shin, T. Yeo, J. Heo, W. Um, Effect of Si/Al molar ratio and curing temperatures on the immobilization of radioactive borate waste in metakaolin-based geopolymer waste form, Journal of Hazardous Materials 458 (2023) 131884. https://doi.org/10.1016/j.jhazmat.2023.131884.
[46] Y. Wang, Y. Cao, Z. Zhang, P. Zhang, Y. Ma, A. Wang, H. Wang, Intrinsic sulfuric acid resistance of C-(N)-A-S-H and N-A-S-H gels produced by alkali-activation of synthetic calcium aluminosilicate precursors, Cement and Concrete Research 165 (2023) 107068. https://doi.org/10.1016/j.cemconres.2022.107068.
[47] E. Kapeluszna, Ł. Kotwica, A. Różycka, Ł. Gołek, Incorporation of Al in C-A-S-H gels with various Ca/Si and Al/Si ratio: Microstructural and structural characteristics with DTA/TG, XRD, FTIR and TEM analysis, Construction and Building Materials 155 (2017) 643–653. https://doi.org/10.1016/j.conbuildmat.2017.08.091.
[48] Z. Fang, X. Xu, X. Yang, H. Xie, X. Zhao, B. Wang, D. Zhao, Y. Yang, Structural stability and aqueous durability of Cs incorporation into BaAl2Ti6O16 hollandite, Journal of Nuclear Materials 565 (2022) 153716. https://doi.org/10.1016/j.jnucmat.2022.153716.
[49] C. Liu, Z. Li, S. Nie, J. Skibsted, G. Ye, Structural evolution of calcium sodium aluminosilicate hydrate (C-(N-)A-S-H) gels induced by water exposure: The impact of Na leaching, Cement and Concrete Research 178 (2024) 107432. https://doi.org/10.1016/j.cemconres.2024.107432.
[50] B. Walkley, J.L. Provis, Solid-state nuclear magnetic resonance spectroscopy of cements, Materials Today Advances 1 (2019) 100007. https://doi.org/10.1016/j.mtadv.2019.100007.
[51] S.A. Bernal, J.L. Provis, B. Walkley, R. San Nicolas, J.D. Gehman, D.G. Brice, A.R. Kilcullen, P. Duxson, J.S.J. van Deventer, Gel nanostructure in alkali-activated binders based on slag and fly ash, and effects of accelerated carbonation, Cement and Concrete Research 53 (2013) 127–144. https://doi.org/10.1016/j.cemconres.2013.06.007.
[52] E. L'Hôpital, B. Lothenbach, K. Scrivener, D.A. Kulik, Alkali uptake in calcium alumina silicate hydrate (C-A-S-H), Cement and Concrete Research 85 (2016) 122–136. https://doi.org/10.1016/j.cemconres.2016.03.009.
[53] J.L. Provis, A. Palomo, C. Shi, Advances in understanding alkali-activated materials, Cement

947 and Concrete Research 78 (2015) 110–125. https://doi.org/10.1016/j.cemconres.2015.04.013.
948 [54] Y. Marcus, Ionic radii in aqueous solutions, Journal of Solution Chemistry 12 (1983).
949 [55] E. Mukiza, Quoc Tri Phung, S.C. Seetharam, T.N. Nguyen, C. Bruggeman, G. De Schutter,
950 Recent advances in immobilization of radioactive cesium and strontium-bearing wastes in
951 alkali activated materials – A review, Journal of Environmental Management 370 (2024)
952 122746. https://doi.org/10.1016/j.jenvman.2024.122746.
953 [56] D. Wang, Z. Zhang, S. Ding, C. Ning, C. Shi, Y. Ma, Q. Ren, Z. Jiang, Nano-structure and
954 sensitivity of self-sensing geopolymer composites containing nano carbon black, Cement and
955 Concrete Composites 160 (2025) 106072. https://doi.org/10.1016/j.cemconcomp.2025.106072.
956 [57] G.K. Sun, J.F. Young, R.J. Kirkpatrick, The role of Al in C–S–H: NMR, XRD, and
957 compositional results for precipitated samples, Cement and Concrete Research 36 (2006) 18–
958 29. https://doi.org/10.1016/j.cemconres.2005.03.002.
959 [58] H. Ma, Y. Tang, H. Lu, W. Chen, N. Li, Q. Li, Revealing the immobilization mechanism of
960 Nd(III) through in-situ C–S–H formation: Status and coordination of Nd, J Am Ceram Soc.
961 109 (2026) e70387. https://doi.org/10.1111/jace.70387.
962 [59] X. Liu, X. Zhao, H. Yin, J. Chen, N. Zhang, Intermediate-calcium based cementitious materials
963 prepared by MSWI fly ash and other solid wastes: hydration characteristics and heavy metals
964 solidification behavior, Journal of Hazardous Materials 349 (2018) 262–271.
965 https://doi.org/10.1016/j.jhazmat.2017.12.072.
966 [60] S. Levchuk, V. Kashparov, V. s Morozova, V. Pavliuchenko, The use of stable Cs and Sr as
967 proxies for the estimation of radionuclide soil-plant transfer factors, Nuclear Physics and
968 Atomic Energy 26 (2025) 75–85. https://doi.org/10.15407/jnpae2025.01.075.
969 [61] Basic XPS information section strontium (Sr) and strontium compounds, (n.d.).
970 https://xpsdatabase.com/strontium-sr-z38-strontium-compounds/?v=55add3d845bf (accessed
971 November 18, 2025).
972 [62] M.G. Blackford, J.V. Hanna, K.J. Pike, E.R. Vance, D.S. Perera, Transmission Electron
973 Microscopy and Nuclear Magnetic Resonance Studies of Geopolymers for Radioactive Waste
974 Immobilization, Journal of the American Ceramic Society 90 (2007) 1193–1199.
975 https://doi.org/10.1111/j.1551-2916.2007.01532.x.
976 [63] C. Chen, H. Liu, Y. Zhang, G. Gu, J. Hu, Micro-assessment of heavy metal immobilization
977 within alkali-activated copper tailings-slag geopolymer, Cement and Concrete Composites 149
978 (2024) 105510. https://doi.org/10.1016/j.cemconcomp.2024.105510.
979 [64] Y. Shirota, K. Niki, H. Shindo, Stabilities of crystal faces of aragonite-type strontianite (SrCO3)
980 and cerussite (PbCO3) compared by AFM observation of facet formation in acid, Journal of
981 Crystal Growth 324 (2011) 190–195. https://doi.org/10.1016/j.jcrysgro.2011.03.033.
982 [65] D.C.D. Andrade, N.S.D.A. Maniçoba, R.O. Sant'ana, F.A.V. Ferreira, C.S. Figueiredo, J.F.
983 Nascimento, L.S. Pereira, O. Chiavone-Filho, Strontium carbonate solubility data in aqueous
984 mixtures of monoethyleneglycol under a carbon dioxide atmosphere, Braz. J. Chem. Eng. 35
985 (2018) 395–402. https://doi.org/10.1590/0104-6632.20180352s20160355.

986

Supplementary materials

For experiments using radioactive nuclides (^{137}Cs, ^{90}Sr), environmental risks were necessarily considered. Therefore, in order to minimize environmental risks as much as possible, the effect of metakaolin (MK) incorporation on leaching behaviors of stable Cs and Sr was also carried out to select the optimal mix proportion of geopolymer for radioactive nuclides retention experiments. This study focused on the retention mechanism of stable and radioactive Cs and Sr on products evolution, rather than the effect of metakaolin incorporation, so the main text of this study only exhibits the comparison of cement and geopolymer regards to immobilizing Cs and Sr.

Metakaolin was supplied by BASF, METAMAX company (UK), with a CaO content below the detection limit. The chemical composition of MK is shown in Table S1. As for sample GeoCs5*, the amount of metakaolin incorporation was 20%, i.e., FA:GGBS:MK=5:3:2. The alkali activator used and preparation method were identical to those used for the samples without metakaolin.

Table S1 Chemical composition of metakaolin (MK)

Compound（wt%）	SiO_2	Al_2O_3	CaO	Fe_2O_3	MgO	TiO_2	K_2O	Na_2O
MK	49.30	42.90	-	0.45	-	1.56	0.11	0.23

Fig.S1 shows key mineralogical and particle size information. From Fig.S1(a), a broad peak can be observed in the XRD pattern of metakaolin, with an anhydrite peak observed around 26°, indicating that metakaolin is predominantly amorphous. The particle size of metakaolin ranges primarily from 0.16 μm to 98.11 μm, with a peak at 2.42 μm, from Fig.S1(b). The D_{50} particle size of MK is approximately 2.75 μm.

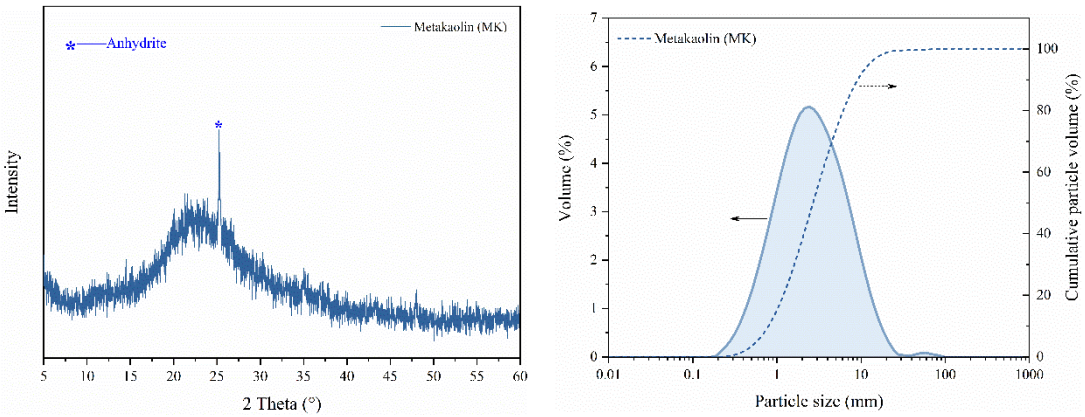

(a) XRD pattern (b) particle size information

1005 Fig.S1 Mineralogical and particle size results for metakaolin (MK) (a) XRD pattern; (b) particle
1006 size information.

1007 Fig.S2 shows the effect of MK incorporation on the leaching behaviors of Cs-containing
1008 samples. From Fig.S2(a), compared with the sample without MK (GeoCs5), the sample with MK
1009 incorporation (GeoCs5*) exhibited lower leaching rates, especially in the early stages of leaching.
1010 From Fig.S2(b), when the leaching period is 42 d, the cumulative fraction leached of samples
1011 GeoCs5 and GeoCs5* leached in Milli Q water are 0.06639 cm and 0.02428 cm, respectively. The
1012 cumulative fractions leached of samples GeoCs5 and GeoCs5* in simulated underground water are
1013 0.07163cm and 0.03319cm. This indicates that the incorporation of metakaolin is beneficial for
1014 immobilization of Cs, regardless of whether leaching occurs in Milli Q water or simulated
1015 underground water.

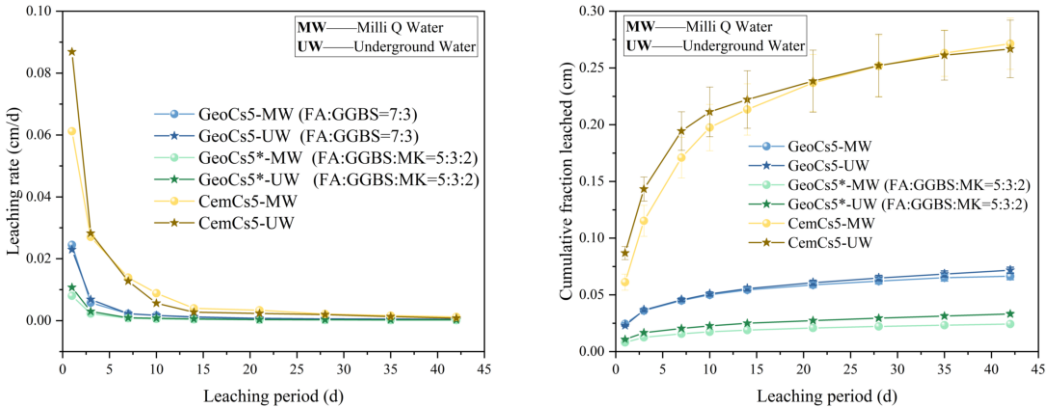

(a) Leaching rate (b) Cumulative fraction leached

Fig.S2 The effect of MK on the leaching behaviors of Cs-containing samples

The leaching model fitting was also performed as shown in Table S2. According to the fitting results, the diffusion coefficient and dissolution rate of samples containing MK are both lower than those of MK-free sample. And for both MK-containing and MK-free samples, the diffusion coefficient and dissolution rate when leached in simulated underground water (UW) are consistently greater than those in Milli Q water (MW).

Table S2 The fitting results of samples containing stable Cs fitted by leaching models.

Sample ID	DFM		DSM		DFM+DSM
	D (cm^2/s)	R^2	U (cm^2/d)	R^2	R^2
GeoCs5-MW	4.80E-10	0.9328	0.000366	0.7872	0.9620
GeoCs5-UW	6.19E-10	0.9497	0.000418	0.8203	0.9718
GeoCs5*-MW	6.96E-11	0.9479	0.000137	0.8159	0.9693
GeoCs5*-UW	1.33E-10	0.9676	0.000193	0.8565	0.9613
CemCs5-MW	1.20E-08	0.9116	0.001823	0.7532	0.9937
CemCs5-UW	8.08E-09	0.8711	0.001462	0.6987	0.9778

Fig.S3 illustrates the impact of MK incorporation on the leaching behavior of Sr-containing samples. As shown in Fig.S3(a), both MK-free and MK-containing samples demonstrated slightly higher initial leaching rates when immersed in Milli Q water compared to those exposed to simulated groundwater. Overall, the leaching profiles showed remarkable similarity during the first 10 days, with minimal differences observed between samples with and without MK incorporation, and samples leached in Milli Q water (MK) versus simulated underground water (UW).

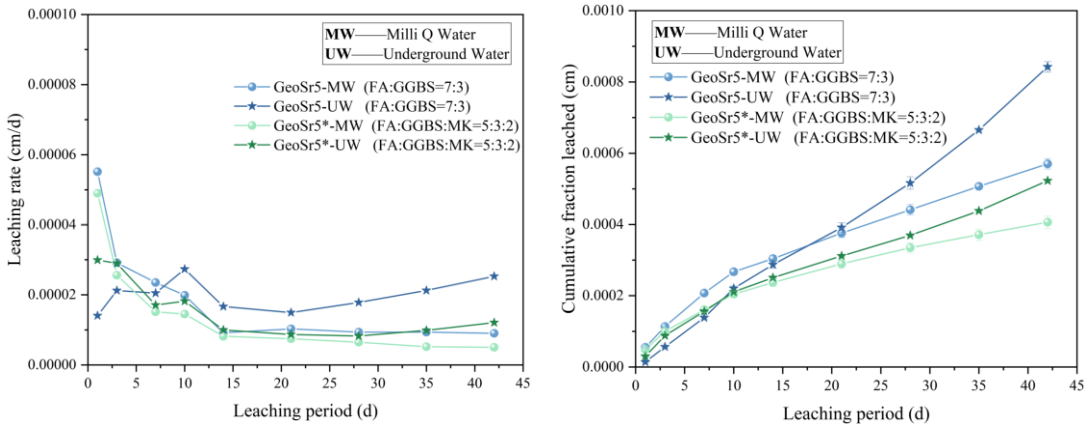

(a) Leaching rate (b) Cumulative fraction leached

1029 Fig.S3 The effect of MK on the leaching behaviors of Sr-containing samples

1030 According to the above results, MK incorporation is beneficial for Cs retention, while there

1031 were no obvious positive effects on Sr immobilization. Therefore, the mix proportion of geopolymer

1032 for radioactive Cs and Sr immobilization were FA:GGBS:MK=5:3:2(GeoCs137*) and FA:GGBS

1033 =7:3 (GeoSr90).

Table 4 Summary of the deconvolution results of 29Si MAS NMR spectra. The RBO (bridging oxygen values), MCL (main chain length) and Si/Al are calculated.

Samples		Q^0	Q^1	Q^2(1Al)	Q^2	Q^3(1Al)	Q^3	Q^4(3Al)	Q^4(2Al)	Q^4(1Al)	Q^4(0Al)	**RBO (%)**	**MCL(NC)**	**MCL(C)**	**Si/Al** NASH	**Si/Al** C(N)ASH
Geo	Pos.(ppm)	-	-	-82.81	-87.06	-91.32	-95.40	-99.90	-105.23	-109.84	-114.62					
	Content(%)	-	-	3.70	10.28	16.99	16.25	18.78	13.88	9.64	10.48	84.70	-	-	2.25	2.78
GeoCs5	Pos.(ppm)	-	-79.37	-85.33	-88.66	-91.93	-95.58	-99.71	-103.89	-108.50	-112.80					
	Content(%)	-	1.56	3.59	6.99	11.80	16.29	16.37	14.76	12.82	15.82	86.51	24.71	133.08	2.61	3.41
GeoCs5-MW	Pos.(ppm)	-72.05	-	-85.63	-89.16	-91.93	-95.81	-99.73	-103.72	-107.70	-111.58					
	Content(%)	0.72	-	5.52	6.43	14.24	17.34	16.39	11.77	10.03	17.55	86.03	-	-	2.70	3.06
GeoCs5-UW	Pos.(ppm)	-72.64	-80.31	-85.96	-89.07	-91.99	-94.97	-99.16	-104.12	-108.61	-113.60					
	Content(%)	1.21	2.74	6.94	11.37	10.60	16.09	17.59	11.36	8.31	13.81	81.90	25.51	85.20	2.44	4.50
GeoSr5	Pos.(ppm)	-70.13	-80.69	-85.53	-88.85	-92.12	-95.56	-99.36	-103.69	-107.52	-111.75					
	Content(%)	2.13	2.63	5.44	8.18	9.48	14.53	16.38	13.44	11.00	16.78	84.89	20.65	75.71	2.65	4.25
GeoSr5-MW	Pos.(ppm)	-75.75	-81.71	-86.16	-89.69	-93.28	-96.79	-100.41	-104.10	-107.68	-111.28					
	Content(%)	2.24	3.08	7.07	11.35	14.39	13.85	14.77	9.59	9.47	14.19	80.99	23.14	83.28	2.63	3.46
GeoSr5-UW	Pos.(ppm)	-75.63	-79.84	-86.05	-89.64	-92.50	-95.92	-100.05	-104.65	-108.78	-112.91					
	Content(%)	2.40	2.72	6.19	6.36	10.23	13.64	13.80	12.10	11.08	21.48	85.36	20.31	72.50	3.05	3.83